Graphical Abstract

Numerical analysis of the rock deformation in twin tunnels with transverse gallery considering plasticity and time-dependent constitutive models

Quevedo, F. P. M.,Colombo, C. A. M. M.,Bernaud, D.,Maghous, S.

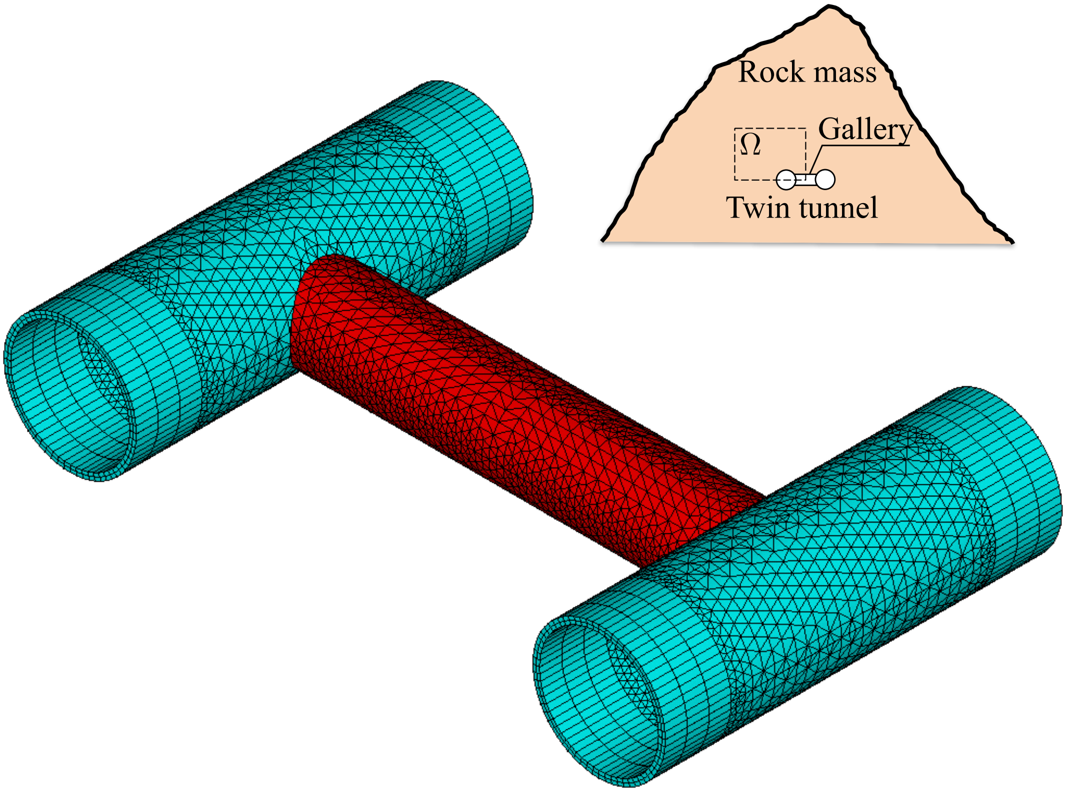

Highlights

Numerical analysis of the rock deformation in twin tunnels with transverse gallery considering plasticity and time-dependent constitutive models

Quevedo, F. P. M.,Colombo, C. A. M. M.,Bernaud, D.,Maghous, S.

- The stiffness of the lining restricting viscous effects in the interaction of tunnels
- Interaction between the tunnels becomes significant at a span distance of 4 radii
- The viscous of the concrete lining can be important in the tunnel convergence
- The effect of the gallery extends into the tunnel up to 4 radii from its axis
- The proximity of the tunnels induces the ovalization of the tunnel wall

Numerical analysis of the rock deformation in twin tunnels with transverse gallery considering plasticity and time-dependent constitutive models

Quevedo, F. P. M.[a,*], Colombo, C. A. M. M.[a], Bernaud, D.[a] and Maghous, S.[a]

[a]*Federal University of Rio Grande do Sul, Av. Osvaldo Aranha, 99, Porto Alegre, 90.035-190, RS, Brazil*

ARTICLE INFO

Keywords:
twin tunnels
transverse gallery
elastoplasticity-viscoplasticity coupling
viscoelastic lining
finite element method

ABSTRACT

Resorting a three-dimensional finite element analysis, this paper investigates the instantaneous and long-term implications induced by the time-dependent constitutive behavior of constituents on the convergence profile of twin tunnels linked with transverse galleries. Several constitutive models for rock mass mechanical behavior are examined at the material level, encompassing elastoplasticity, viscoplasticity, or coupled elastoplasticity-viscoplasticity frameworks. Plasticity state equations are based on a Drucker-Prager yield surface with an associated flow rule, while the viscoplasticity formulation relies on the Perzyna model with a Drucker-Prager flow surface. Tunnel lining behavior is modeled using either elastic or viscoelastic constitutive models. The viscoelastic behavior is described by a Generalized Kelvin rheological model based on Bazant and Prassanann's Solidification Theory, with model parameters derived from CEB-FIP MC90 formulations. From a computational viewpoint, the deactivation-activation method is employed to simulate the excavation process and lining installation. The accuracy of finite element predictions is assessed through comparisons with available analytical solutions formulated in a simplified setting for the twin tunnels' configuration. A parametric study delves into the mutual interaction induced by tunnels proximity, emphasizing the crucial role of concrete lining stiffness in twin tunnels' deformation. Numerical simulations indicate a highly localized influence of a transverse gallery on twin tunnels deformation, extending up to four radii from each side of the gallery axis. Finally, the paper investigates the effects of twin tunnels proximity and those induced by an interconnecting gallery on the instantaneous and long-term convergence of tunnels, contrasting these outcomes with the convergence of a single tunnel.

1. Introduction

Tunnels are critical engineering structures designed to overcome natural barriers like mountains and maritime channels, enabling efficient transportation of people and resources. In urban areas, they optimize space by supporting subway systems and essential infrastructure services such as water, sewage, gas, and electrical networks. Their role extends to specialized applications in hydroelectric plants, underground labs, radioactive waste storage, mining, and petrochemical industries. As a key technology, tunnels address complex geotechnical and structural challenges, contributing significantly to national infrastructure and development.

The structural design and analysis of tunnels require consideration of numerous geotechnical parameters and the accurate estimation of several critical factors such as tunnel convergence (or closure), the pressure in tunnel lining, and plastification of the surrounding rock mass. For shallow tunnels, surface settlement also becomes a significant concern. The stress and deformation fields that develop around a tunnel are influenced by the tunnel's depth, the tunnel wall geometry, anisotropy of in situ stresses, presence of water, and surface structures in the case of shallow tunnels. Additionally, the excavation method and lining installation play crucial roles, as does the rheological behavior and coupling of both the rock mass and the lining.

*Corresponding author.

motta.quevedo@ufrgs.br (Q.F.P. M.); ca-colombo@hotmail.com (C.C.A.M. M.); denise.bernaud@ufrgs.br (B. D.); samir.maghous@ufrgs.br (M. S.)

https://www.researchgate.net/profile/Felipe-Pinto-Da-Motta-Quevedo (Q.F.P. M.); http://lattes.cnpq.br/4919388217690564 (C.C.A.M. M.); http://lattes.cnpq.br/2809615143819128 (B. D.); https://www.researchgate.net/profile/Samir-Maghous (M. S.)

ORCID(s): 0000-0003-4171-1696 (Q.F.P. M.); 0000-0001-6365-3269 (B. D.); 0000-0002-1123-3411 (M. S.)

A key challenge in tunnel modeling is capturing the interaction between short-term and long-term structural behavior. The time-dependent behavior can greatly impact deformations and the overall stability of the tunnel. Short-term response such as rock mass plasticization, tunnel wall closure, and loading on the lining may develop not only during tunnel construction but also progressively over months or even years.

In adjacent tunnels such the twin tunnels, there is also the interaction due to the proximity of the tunnels, lagging distance between escavation faces and, if present, transverse galleries, which cause localized stress distribution and overloading the main tunnels. Furthermore, unlike single tunnels, twin tunnels with gallery can only be studied with three-dimensional models.

Most investigations on adjacent or twin tunnels focus on shallow tunnels (e.g., [1, 2, 3, 4, 5] to cite a few recent ones). Ground settlement and interaction with surface structures are typical concerns for urban metro systems. Since the present study is only interested in deformation fields at gallery's influence zone considering nonlinear and time-dependent constitutive models, for simplicity, only deep twin tunnel domain is consdered. A comprehensive review on ground settlements involving twin tunnels can be found in [6]. For deep twin tunnels, some recent investigations are presented below.

Regarding to analytical formulations, Chen et al. [7] developed a solution using complex variables, Fourier transformation, and the alternating Schwarz method, considering rock mass and lining in elasticity. Their findings show that the interaction between adjacent tunnels vanishes when the spacing exceeds six times the tunnel radius and the lining significantly reduces the stress concentration, especially at high lateral stress coefficients.

Ma et al. [8] proposed an analytical method, verified by a numerical solution using FLAC3D software for determining the plastic zones around deep circular twin tunnels without linings, restricting themselves where there is no overlap between the two plastic zones. In this case, the authors adopted the elastoplastic perfectly constitutive model for the homogeneous and isotropic rock mass, with the Mohr-Coulomb criterion. Also carried out parametric studies to understand the influence of the distance between the twin tunnels, cohesion, the angle of internal friction, and the vertical and horizontal initial stresses acting on the shape and depth of the plastic zones. These authors stated that the plastic zone around the tunnel provides a relevant theoretical basis for defining and designing the support. In that respect, an excessive plastic zone would significantly affect the stability and functionality of a tunnel. Reducing the extension of the plastic zone around tunnels is, therefore, of significant importance in engineering tunnel design projects.

Guo et al. [9] develop an elastic analytical solution for the stress field around twin circular tunnels under hydrostatic pressure using the complex variable and the superposition principle. They found that tangencial stress in tunnel wall increased as the distance between the parallel tunnels decreased and the supporting pressure leads to the radial stress increasing and the tangential stress decreasing.

According to Fortsakis [10], in a realistic construction context, twin tunnels are excavated and supported with a delay, so that the second tunnel is usually built after the first one has advanced enough to maintain a longitudinal separation distance between the faces. Trought numerical model, considering a perfect elastoplastic rock mass with Mohr-Coulomb criterion and a linear elastic lining, he concluded that the advance of the subsequent tunnel mobilizes the redistribution of stresses and deformations in the zone between the tunnels, resulting in additional loading of the preceding tunnel.

Chortis and Kavvadas [11] carried out parametric 3D finite element analyses to verify the interaction between deep twin tunnel, with circular and non-circular cross-section, supported by a shotcrete elastic linear lining. Was considering the rock mass with linear elastic behavior and perfectly plastic, with Mohr-Coulumb failure criteria. The study investigates the axial forces that develop in the primary lining of the twin tunnels as a function of the main geometric and geomaterial parameters, but without considering the potential time-dependent deformations (creep effect) that occur in some types of rock masses.

In another study but same constitutive models, Chortis and Kavvadas [12] examined the axial forces acting on the primary support in the perpendicular intersection zone between two deep tunnels. The results of the analysis indicated that the zone of influence extends approximately two diameters from the main tunnel to each side from the center of the intersection and that the interaction effects are practically eliminated when they exceed this influence zone. During the construction of the transverse tunnel, the surrounding rock mass is subjected to a redistribution of stresses, causing an additional load on the main tunnel, precisely in the intersection zone. If these additional loads exceed the load capacity of the primary support of the main tunnel, a potentially unstable region can develop, leading to failure, especially in adverse geotechnical conditions.

Using parametric three-dimensional numerical analyses, Chortis and Kavvadas [13, 14] investigated the effect of building a transverse tunnel that intersected deep twin tunnels perpendicularly, focusing the study on the axial forces and the circumferential and longitudinal bending moments acting on the primary support of the intersection regions, respectively. The constitutive model of the rock mass was a perfect elastoplastic following the Generalised Hoek-Brown failure criterion while the shotcrete a linear elastic material. According to the authors, the critical zone in the primary support of the main tunnel extends approximately one diameter from the main tunnel, on both sides of the centre of the intersection.

In this context, the main contributions of this paper may be summarized at both the material and tunnel analysis levels. At the material level, the constitutive state equations of the rock mass are formulated within the framework of coupled plasticity-viscoplasticity, which is relevant for clayey rocks. Such a framework allows capturing the irreversible instantaneous tunnel response (plasticity) as well as the delayed irreversible response (viscoplasticity). As regards the mechanical behavior of concrete material defining the lining, which is classically modeled through linear elastic relationships, the present analysis considers an aging viscoelastic rheological model relying upon the Bažant and Prasannan Solidification theory [15, 16]. At the structure analysis level, the simulation of deformation in the highly interacting material system components (namely, rock mass and lining), resulting from the excavation process of twin tunnels and transverse gallery, is handled using finite element simulations performed in a three-dimensional setting. From the computational viewpoint, the excavation process and lining placement are simulated by means of the activation/deactivation technique. The constitutive models formulated for the rock mass and lining constituent as well as the related numerical integration schemes are implemented into the same procedure UPF/USERMAT customization tool [17] of ANSYS standard software. The three-dimensional finite element analysis developed in this paper is specifically devised for addressing the three-dimensional interaction induced by the construction process, twin tunnels proximity, and the presence of the transverse gallery.

In sequence, the outlines the study's fundamental assumptions and limitations are summarized, followed by the presentation of constitutive models for the rock mass and lining, and the spatial and time discretization for the numerical application. However, before this application, preliminary simulations and verifications with analytical solutions will be presented. Next, the numerical application will then be presented and discussed. This study investigates the effect of the gallery's presence and twin tunnel proximity on convergence profiles, incorporating nonlinear and time-dependent behavior in the rock mass and lining.

2. Fundamental assumptions

The basic assumptions of the constitutive and computational modeling, as well as related limitations, are summarized as follows:

(a) Only the configuration of deep tunnels shall be considered in the subsequent analysis, thus neglecting deformations caused by surface loads and settlements arising from the excavation process.

(b) Although material heterogeneity and behavior anisotropy are inherent features of soils and rocks, the rock mass is modeled throughout the paper as a homogeneous and isotropic continuous medium. At the scale adopted for tunnel modeling (macroscopic scale), this assumption means in particular that the possible micro-heterogeneities, such isotropic distributions of joints or cracks present at the finer scale, are accounted for in the homogenized behavior by means of a preliminary homogenization process (e.g., [18, 19, 20, 21, 22]). Clearly enough, the framework of continuum modeling adopted in the paper would reveal questionable when the rock mass is cut by a few macroscale fracture joints.

(c) The rock mass is phenomenologically modeled using an elastoplastic-viscoplastic rheological law to capture instantaneous and long-term responses. This approach disregards the aspect connected temperature gradients, water flow, and poromechanics coupling.

(d) Despite the complexity of the stress distribution prevailing in the rock mass before the process of tunnel excavation, which is mainly affected by the geological history, the present study assumes a geostatic initial stress reflected by vertical and horizontal stresses.

(e) Twin tunnels are often designed considering a time gap between excavation fronts. However, the finite element simulations assume synchronous excavation steps to ensure symmetry conditions.

(f) The simulation excavation processes are curried out assuming a constant tunnel advancement rate (i.e., constant excavation speed), together with a constant thickness of concrete lining.

(g) Effects of temperature and humidity that may affect the viscoelastic behavior of lining concrete are disregarded.
(h) Perfect bonding is assumed at the interface between concrete lining and the rock mass.
(i) The framework of infinitesimal strain analysis, together with quasi-static evolutions, is adopted in the paper. In particular, dynamic excitations and related inertial forces, such as those induced, for instance, by earthquakes or explosions, shall not be considered in the numerical analysis.

3. Constitutive Model of the Rock Material

Time-dependent phenomena associated with the delayed behavior of the constitutive material are key aspects of deformation in tunnel structures excavated in deep clayey rocks (see for instance [23, 24] or [25], to cite a few). In most computational analyses developed for tunnel engineering design, this issue is generally addressed by means of viscoplastic constitutive behavior. While such constitutive models could relevantly model the transient and long-term deformation, they seem however inadequate to capture the influence of short-term events (tunnelling and support placement phases) on the final stability of the structure. In particular, an analysis of tunnel deformation based on a viscoplastic model would suggest that the ultimate support pressure at tunnel structure equilibrium mainly depends on the closure rate at the moment when the contact between lining and rock mass is achieved (e. g., [24]), thus disregarding the irreversible effects rising in the initial construction phases. Indeed, during the primary stages of tunnel excavation, the surrounding rock mass is subjected to severe loading conditions and high strain rates, which may lead to yielding associated with high instantaneous irreversible strains near the tunnel wall, and can therefore affect the long-term equilibrium of the structure. It is thus of fundamental concern to formulate a constitutive model that incorporates both instantaneous and delayed irreversible components of the rock material. For this purpose, the present analysis considers a constitutive model that includes both instantaneous plasticity to describe shorth-term material yielding and viscoplasticity to represent delayed behavior. The formulation of the coupled plasticity-viscoplasticity rheological model is based on that originally proposed in [24] and [23]. Previous studies have implemented this plastic-viscoplastic model for computational analysis of deformation in single tunnels (e.g., [26, 27, 25, 28]. For the sake of brevity, only the main features of this constitutive model shall be summarized below. Detailed description of the model, including application and validation in the context of single tunnel structures may be found in [29]. Finite element implementation of this model in the USERMAT procedure of ANSYS software is also described in [28].

The elastoplastic-viscoplastic model is formulated based on a serial association of the elastoplastic and viscoplastic constitutive models. The local strain rate $\dot{\boldsymbol{\varepsilon}}$ is split into three contributions $\dot{\boldsymbol{\varepsilon}} = \dot{\boldsymbol{\varepsilon}}^e + \dot{\boldsymbol{\varepsilon}}^p + \dot{\boldsymbol{\varepsilon}}^{vp}$, so that the constitutive relationships relating the Cauchy stress rate $\dot{\boldsymbol{\sigma}}$ and strain rate components can be written as:

$$\dot{\boldsymbol{\sigma}} = \boldsymbol{D} : \dot{\boldsymbol{\varepsilon}}^e = \boldsymbol{D} : (\dot{\boldsymbol{\varepsilon}} - \dot{\boldsymbol{\varepsilon}}^p - \dot{\boldsymbol{\varepsilon}}^{vp}). \tag{1}$$

In the above relationship, $\dot{\boldsymbol{\varepsilon}}^e$, $\dot{\boldsymbol{\varepsilon}}^p$ and $\dot{\boldsymbol{\varepsilon}}^{vp}$, represent respectively the elastic, plastic and viscoplastic strain rate, and $\boldsymbol{D}$ denote the fourth-order isotropic elastic linear constitutive tensor. Tensor $\boldsymbol{D}$ is defined by the rock mass elastic Young modulus E and Poisson ratio ν. The one-dimensional representation of the constitutive behavior is shown in Fig. 1.

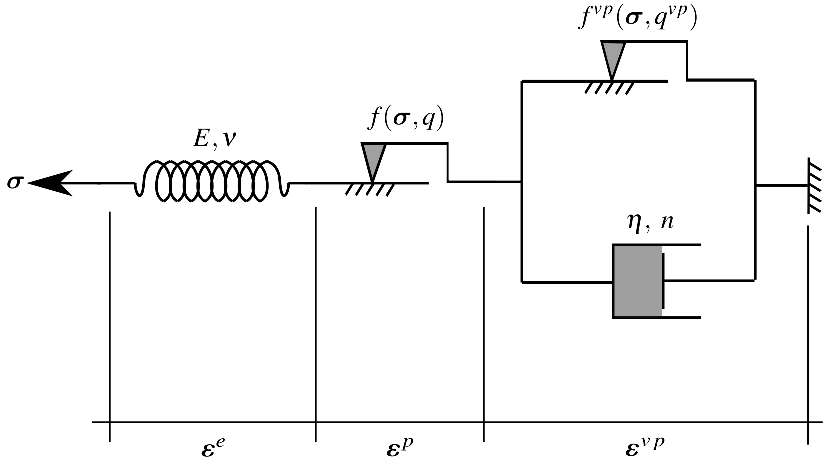

Figure 1: Rheological representation of the elastoplastic-viscoplastic model.

In the three-dimensional context, the plasticity component of constitutive behavior is described by a Drucker-Prager plastic flow surface given by:

$$f(\boldsymbol{\sigma}, q) = f(I_1, J_2, q) = \beta_1 I_1 + \beta_2 \sqrt{J_2} - q(\alpha), \tag{2}$$

which I_1 is the first invariant of the stress tensor, J_2 the second invariant of the deviator tensor and β_1, β_2 and $q(\alpha)$ are strength parameters related to the friction angle ϕ and cohesion $c(\alpha)$, respectively. Drucker-Prager plasticity surface inscribed to the Mohr-Coulomb surface shall be considered throughout the subsequent analysis [30]:

$$\beta_1 = \frac{(k-1)}{3}, \quad \beta_2 = \frac{(2k+1)}{\sqrt{3}}, \quad q(\alpha) = 2\sqrt{k}\, c(\alpha), \tag{3}$$

where $k = (1 + \sin\phi)/(1 - \sin\phi)$. The internal variable α is the equivalent plastic strain $\bar{\varepsilon}^p$ used to simulate strain hardening/softening phenomena. However, for this study, we adopt perfect plasticity, meaning that c is a constant. For the viscoplasticity surface f^{vp} the same surface is empolyed, but with ϕ^{vp} in β_1 and β_2, and $q^{vp} = 2\sqrt{k^{vp}} - c^{vp}$ where $k^{vp} = (1 + \sin\phi^{vp})/(1 - \sin\phi^{vp})$ and c^{vp} is a constant, i.e., perfect viscoplasticity. The plastic flow rule is given by:

$$\dot{\boldsymbol{\varepsilon}^p} = \begin{cases} \dot{\lambda}\dfrac{\partial g}{\partial \boldsymbol{\sigma}} & \text{for } f > 0 \\ \mathbf{0}, & \text{for } f \leq 0 \end{cases}, \tag{4}$$

where $\dot{\lambda}$ is the plasticity multiplier and g is a potential flow function analogous to f used to simulate the volume dilatation during the evolution of plastic deformations. However, for this analysis, was used associated plasticity, i.e., $g = f$. The plastic multiplier is obtained through the consistency condition $\dot{f} = 0$. Numerical details of this implementation can be found in [29]. For viscoplastic flow rule we have,

$$\dot{\boldsymbol{\varepsilon}}^{vp} = \dot{\lambda}^{vp} \frac{\partial f^{vp}}{\partial \boldsymbol{\sigma}} \tag{5}$$

In contrast to the plastic multiplier, the viscoplastic multiplier λ^{vp} is independent of a consistency like condition. As a result, its expression is explicit. Based on the framework of generalized Perzyna's overstress theory [31], its expression may be derived as follows:

$$\dot{\lambda}^{vp} = \frac{\Phi(\boldsymbol{\sigma}, q^{vp})}{\eta} \quad \text{and} \quad \Phi = \left\langle \frac{f^{vp}(\boldsymbol{\sigma}, q^{vp})}{f_0} \right\rangle^n, \tag{6}$$

where Φ is the overstress function, η is the dynamic viscosity constant, n is the dimensionless parameter that gives the form of the power law, f_0 a parameter conveniently adopted and $\langle * \rangle$ is the McCauley function which is 0 when $* < 0$, i.e. viscoplastic flow will only occur when the overstress function is positive.

In this coupled model, when $\phi = \phi^{vp}$, cohesion entirely controls the evolution of local mechanical fields. Specifically, when $c \to \infty$ and $c^{vp} \to \infty$, the system achieves a purely elastic solution. The solution becomes purely elastoviscoplastic with $c \to \infty$, while a pure elastoplastic solution emerges with $c^{vp} \to \infty$. In the coupled analysis, condition $c^{vp} < c$ is adopted, allowing the viscoplastic domain to occur without plasticity. However, in the presence of plasticity, viscous effects become inevitable. Fig. 2 illustrates these domains in principal stress space.

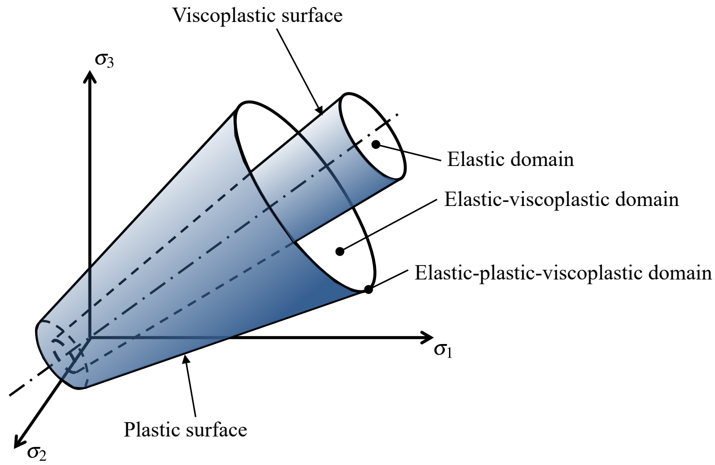

Figure 2: Elastoplastic-viscoplastic domains.

4. Constitutive Model of the Lining

Shrinkage and creep phenomena represent fundamental components of concrete deformation processes that are expected to naturally affect the instantaneous as well as the transient and long-term behavior of structures involving such material. However, most of the tunnel design analyses consider the concrete involved in lining systems as a linear elastic material. From a phenomenological point of view, creep of concrete refers to the time-dependent deformation induced by sustained loading, whereas shrinkage deformation refers to the volume decrease caused by drying. As far as deformation in tunnel structures is concerned, creep and shrinkage have an important effect on the performance of the concrete lining and consequently on its contribution to controlling the long-term convergence of the tunnel. To account for such constitutive features, the concrete creep deformation is addressed by means of an aging viscoelastic rheological model relying on Bažant and Prasannan Solidification Theory [15, 16]. The viscoelastic model is described by a Generalized Kelvin-chain as depicted in Fig. 3. The mechanical parameters that define such a rheological model are the springs stifness and dash-pots viscosity. The model parameters are calibrated based on the CEB-FIP MC90 standard specifications formulation reported in [32]. One may refer to [33 , 34] for detailed description of the calibration procedure. As regards the concrete deformation associated with shrinkage, the isotropic formulation proposed in CEB-FIP MC90 standard [32] is adopted in the present modeling and subsequent computational analyses. Full details regarding model definition and related finite element implementation may be found in [35] and [34].

Accordingly, the constitutive equations for concrete lining relating the stress and strain rate can be expressed in the framework of infinitesimal strain analysis as:

$$\dot{\boldsymbol{\sigma}} = \boldsymbol{D} : \dot{\boldsymbol{\varepsilon}}^{e} = \boldsymbol{D} : \dot{\boldsymbol{\varepsilon}} - \boldsymbol{D} : \dot{\boldsymbol{\varepsilon}}^{sh} - \boldsymbol{D}^{*} : \dot{\boldsymbol{\varepsilon}}^{cr} \tag{7}$$

In the above relationship, $\dot{\boldsymbol{\varepsilon}}^{sh}$ and $\dot{\boldsymbol{\varepsilon}}^{cr}$ are respectively the shrinkage and creep strain rates. The fourth-order tensors $\boldsymbol{D}$ and $\boldsymbol{D}^{*}$ refer to the isotropic elastic linear constitutive tensor and modified constitutive tensor that incorporate the aging viscoelastic properties of the concrete, respectively.

For the numerical implementation purposes, relationship (12) may conveniently be written in incremental form:

$$\Delta\boldsymbol{\sigma} = \boldsymbol{D} : \Delta\boldsymbol{\varepsilon} - \boldsymbol{D} : \Delta\boldsymbol{\varepsilon}^{sh} - \boldsymbol{D}^{*} : \Delta\boldsymbol{\varepsilon}^{cr} \tag{8}$$

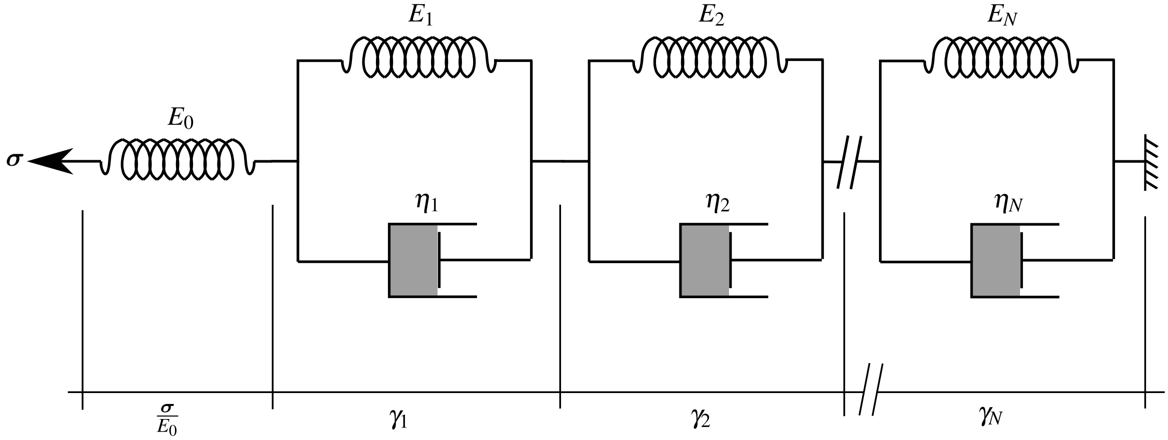

Figure 3: Generalized Kelvin model for uniaxial concrete viscoelasticity.

As mentioned above, isotropic formulation is considered for shrinkage, so that increment of shrinkage strain reads:

$$\Delta \boldsymbol{\varepsilon}^{sh} = \Delta \varepsilon_{sh}(t_s)\mathbf{1} \tag{9}$$

where t_s represents the concrete curing time, and $\Delta\varepsilon_{sh}$ is the variation in magnitude of the concrete deformation associated with shrinkage (the dependency $\Delta\varepsilon_{sh}$ of on current time is omitted). The latter expression is determined based on CEB-FIP MC90 standard specifications [32].

Regarding the increment of creep strain $\Delta\boldsymbol{\varepsilon}^{cr}$, its value is computed making use of the incremental algorithm developed by Bažant and Prasannan [15, 16], together with a model calibration that incorporates CEB-FIP MC90 standard formulation [32]. More precisely, the three-dimensional ageing viscoelastic behavior of isotropic concrete is defined by the Generalized Kelvin model for the relaxation modulus under uniaxial stress, whereas the Poisson ratio is assumed to be time independent within the time interval of analysis. The procedure for the identification of model parameters is achieved by comparing the creep functions provided in references [15, 16] and [32], leading to the following equivalence:

$$E_0 = E_c(t_0),\ \gamma(t-t_0) = \beta_c(t-t_0),\ \frac{1}{v(t)} = \frac{\phi_0(t_0)}{E_{ci}} \text{ and } \frac{1}{\eta(t)} \to 0 \tag{10}$$

in which t refers to the current time value and t_0 to the concrete age at the instant of load application (time interval $t-t_0$ is generally referred to as loading time or loading age). In the Generalized Kelvin model introduced by Bažant and Prasannan [15, 16], E_0 is the instantaneous elasticity modulus of the concrete formed aggregates and cement paste particles, $\gamma(t-t_0) = \sum_{i=1}^{N} \gamma_i$ is the microviscoelastic deformation of the volume fraction $v(t)$ of solidified concrete and $\eta(t)$ is the apparent macroscopic viscosity. In the CEB-FIP MC90 formulation [32], $E_c(t_0)$ stands for the tangent elastic modulus of concrete at the instant of the loading application t_0, $\beta_c(t-t_0)$ is a coefficient that depends on the loading age $t-t_0$, $\phi_0(t_0)$ is a coefficient defining the delayed strain when loaded at age t_0 of the concrete, and E_{ci} represents the tangent elasticity modulus of the concrete at the age of 28 day.

5. Spatial and time discretization of the domain

The geometry model of analyzed domain Ω is schematically displayed in Fig. 4. It consists of a system of deep twin tunnels connected with a transverse gallery. The radius of the circular longitudinal tunnels is denoted by R_t, whereas that of the circular connecting gallery is denoted by $R_g \leq R_t$. The underground structure is excavated in a homogeneous rock mass at great depth $H \gg R_t$.

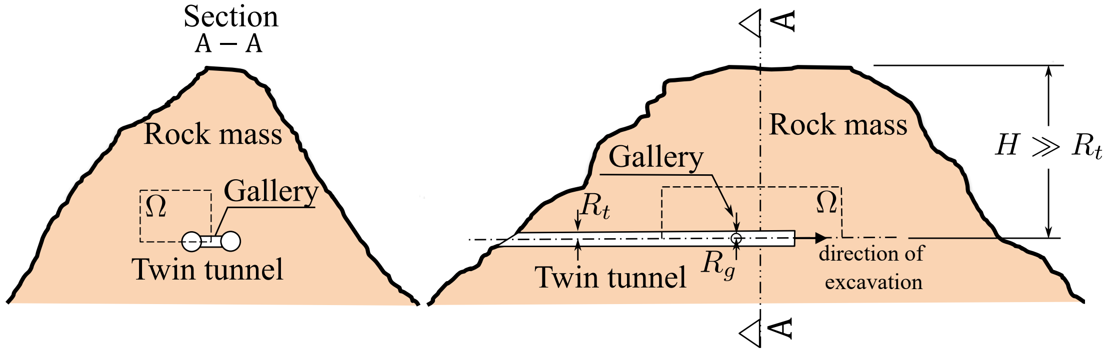

Figure 4: Schematic representation of the twin tunnels geometry problem.

Within the analyzed material domain, the initial stress state prevailing in the rock mass prior to the tunnel excavation process is defined by constant vertical and horizontal geostatic stress σ_v and σ_h, taking the following form:

$$\boldsymbol{\sigma}_0 = -\sigma_v \boldsymbol{e}_y \otimes \boldsymbol{e}_y - \sigma_h \left(\mathbf{1} - \boldsymbol{e}_y \otimes \boldsymbol{e}_y\right) \tag{11}$$

where is the upward unit vector parallel to vertical direction. The initial horizontal stress is generally related to the vertical stress by means of the horizontal thrust coefficient $\sigma_h = k_0 \sigma_v$. Starting from the initial configuration of the material system Ω, the processes of excavation (advancing face) and lining placement are simulated by means of the "activation/deactivation" technique [36, 37, 38, 34].

The geometry material domain Ω considered for the finite element simulations, including tunnelling and deformation analysis, is defined by a parallelepiped volume of dimensions $\left(L_1 + L_2\right) \times L_3 \times d_3$ (Fig. 5). Owing to the symmetry of the problem, only the material domain $\{x \leq 0, y \geq 0\}$ is considered for F.E discretization and analysis. Referring to the notations of Fig. 5, d_1 is the distance between the axes of longitudinal tunnels, L_2 represents the total length along longitudinal direction $\boldsymbol{e}_z$ of the cylindrical volume to be excavated that is considered in the numerical simulation, d_3 is the thickness along vertical direction $\boldsymbol{e}_y$ of material domain Ω, L_1 stands for the length of unexcavated region after total excavation process, L_3 is the total length along transversal direction $\boldsymbol{e}_x$ of discretized material domain, d_2 characterizes the location of the circular transverse axis gallery that intersects the longitudinal tunnel at $z = L_1 + d_2$. The length of the excavation step adopted will be denoted by L_{pt}. The finite element model including geometrical discretization and boundary conditions is illustrated in Fig. 5. The mesh used in the simulations consists of 119740, 182470 or 221104 total elements (hexahedra and tetrahedra), depending on the value of spacing between longitudinal tunnels. To increase the accuracy of the model predictions in the intersection zone, the region surrounding the transverse gallery (including part of the longitudinal tunnel) is discretized by means 10-node quadratic tetrahedral elements, whereas 8-node trilinear hexahedral elements are used for the remaining part of the structure. Furthermore, a refined meshing is used for discretizing the zones surrounding the longitudinal and transverse gallery. These zones whose mechanical state is significantly affected by the tunnelling process are indicated by light gray color in Fig. 5.

Figures 6 to 10 display some details regarding the geometry and F.E discretization of the structure. Fig. 6 presents some details of the longitudinal tunnel cross-section in a xy plane, together with the layer of concrete lining (in sky blue color), parameter e_t being the thickness of the lining. Installation of the lining (shotcrete or precast concrete) is simulated in the F.E modeling by progressive activation of the corresponding elements, which consists in assigning to these elements the concrete mechanical properties.

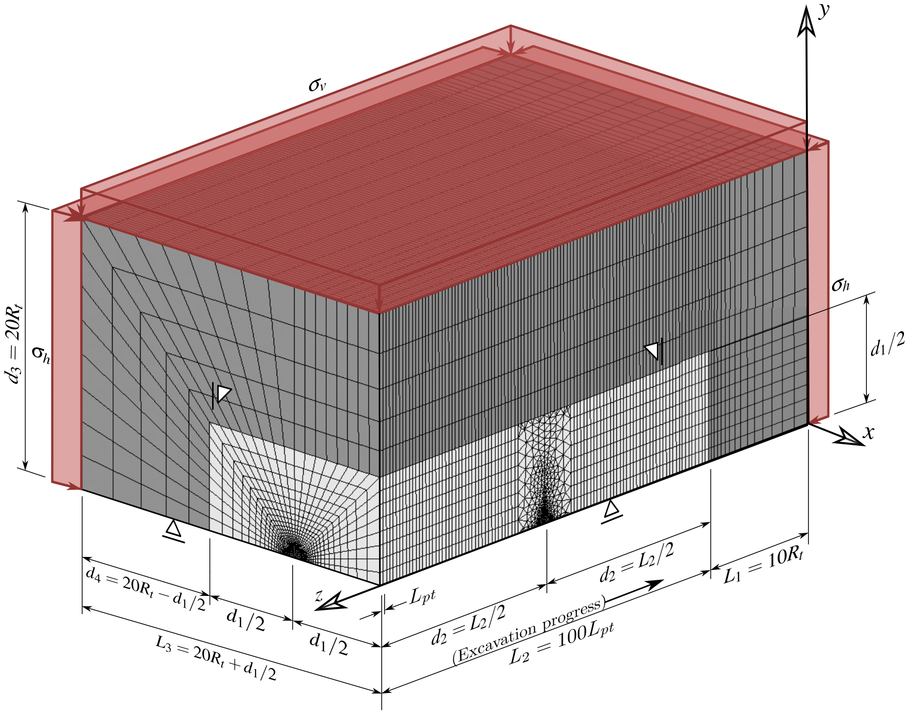

Figure 5: Mesh, dimensions and boundary conditions of the 3D twin tunnel domain.

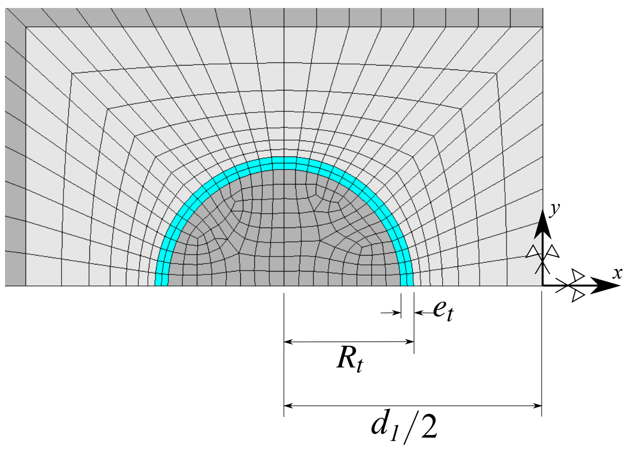

Figure 6: Detail 1 - Mesh in longitudinal tunnel cross-section with spacing $d_1 = 4R_t$.

An important issue investigated in this work is the influence of the spacing d_1 between twin tunnels on their convergence. Fig. 7 and Fig. 8 illustrate the spatial discretization of the gallery region as well as of the connection with the longitudinal tunnel. Three values shall be considered for the spacing d_1 in the numerical simulations, namely $d_1 = 16R_t, 8R_t$ and $4R_t$. The layer of concrete lining of thickness e_g installed along the gallery wall is indicated by red color in the figures. Without introducing additional modeling restriction and for the sake of simplicity, the value of the gallery radius is fixed to $R_g = 2/3R_t$. The same lining system (same concrete material and layer thickness) is considered for both longitudinal tunnels and gallery. As regards the discretization of the region surrounding the gallery, parameters d_5 and d_1 define the size in a yz plane of the transition region involving the tetrahedral finite elements. Fig. 9 provides a view of the transition region and tunnel/gallery intersection zone.

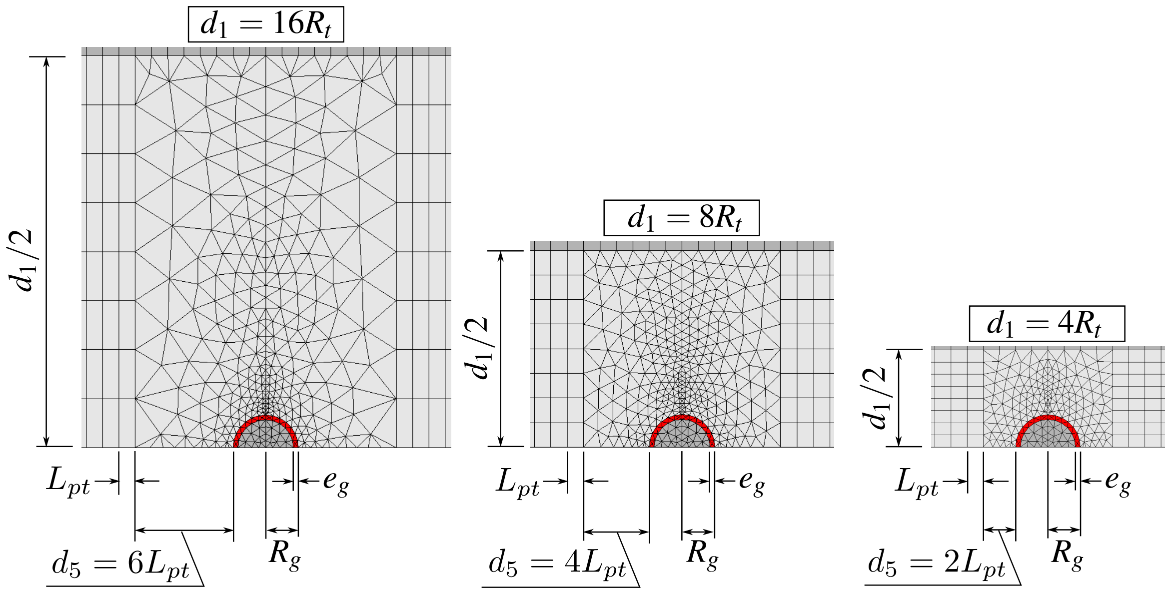

Figure 7: Geometry and F.E mesh of gallery cross-section for configurations $d_1 = 16R_t$, $d_1 = 8R_t$ and $d_1 = 4R_t$.

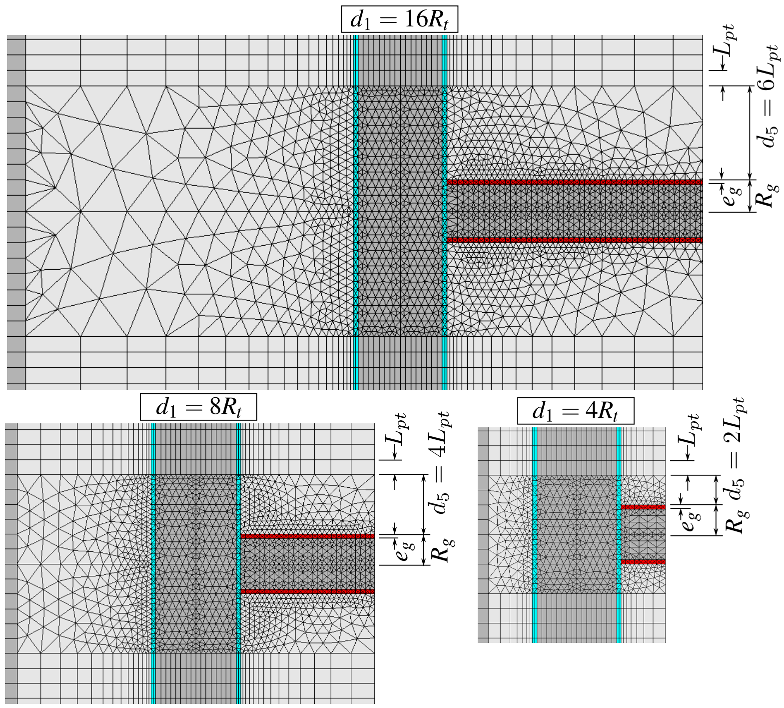

Figure 8: Views of longitudinal tunnel and gallery in the symmetry plane $y = 0$ for configurations $d_1 = 16R_t$, $d_1 = 8R_t$ and $d_1 = 4R_t$.

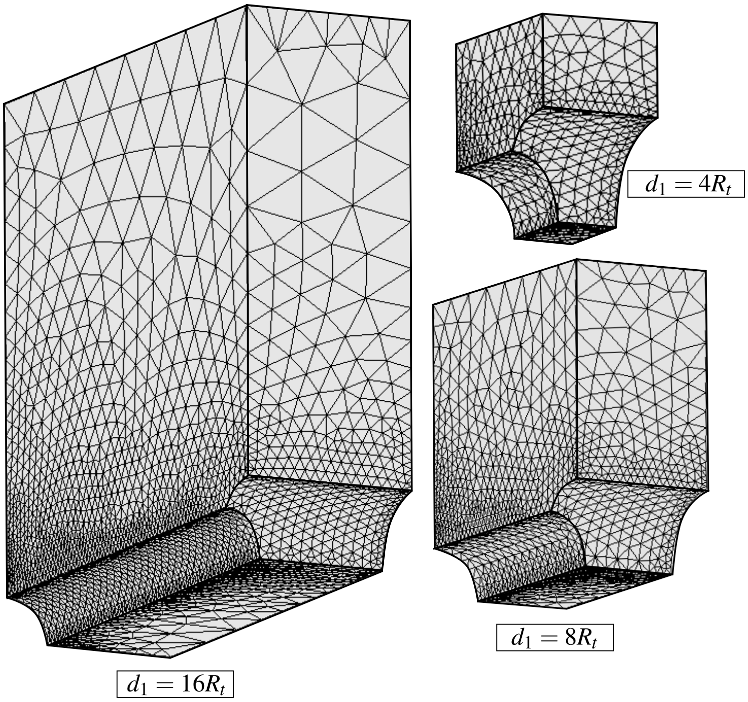

Figure 9: View of the transition and tunnel/gallery intersection zones for configurations $d_1 = 16R_t$, $d_1 = 8R_t$ and $d_1 = 4R_t$.

Finally, Fig. 10 presents the F.E mesh used for the layer of concrete lining in both the longitudinal layer (in sky blue color) and the gallery (in red color) for the three configurations $d_1 = 16R_t$, $d_1 = 8R_t$ and $d_1 = 4R_t$, with specific details on the junction region of the gallery and the longitudinal tunnel. For the illustration purposes, symmetry with respect to plane $y = 0$ has been used to complete the geometry representation of each configuration. It is emphasized that the tetrahedral elements used for the discretization of the region surrounding the transverse gallery exactly fits excavation steps (elements removal or deactivation).

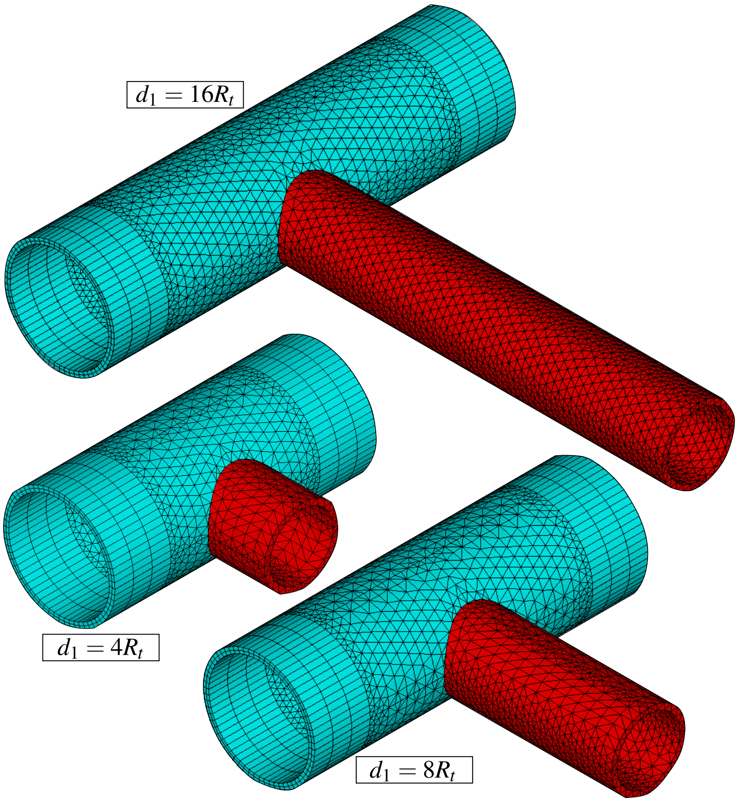

Figure 10: Isometric view of the lining at the intersection for $d_1 = 16R_t$, $d_1 = 8R_t$ and $d_1 = 4R_t$ - expansion of symmetry in the xz plane.

As mentioned previously, the tunnelling process, including the excavation steps and lining installation, is simulated resorting to the activation-deactivation method. Each excavation step is modeled by deactivation of the corresponding elements (the elements stiffness is reduced by a factor $1E8$), whereas installation of elements of lining at a distance d_{0t} from the excavation face (unlined length) is achieved through activation of the corresponding elements by assigning them concrete properties. The F.E solution of the time-dependent problem is performed for each excavation step associated with time interval $t_p = L_p/V_p$, where L_{pt} represents the length of the excavation step and V_{pt} is the speed of the excavation face. Fig. 11 schematically displays the consecutive phases of excavation process. In this Figure, n_p is the total number of excavation steps and n_{pig} represents the number of longitudinal tunnel excavation steps prior to gallery excavation. After achievement of the n_{pig} excavation steps, the excavation of the gallery is initiated starting from the longitudinal tunnel wall. Referring to the notation of Fig. 11, L_{pg} is the considered step length for the gallery excavation, V_{pg} is the speed of the gallery excavation, and d_{0g} is the unlined length of the gallery. Each gallery excavation step is associated with time interval $t_{pg} = V_{pg}/L_{pg}$. After the gallery excavation is completed, we proceed to further excavation steps of the longitudinal tunnel.

For the sake of clearness, the main parameters defining the geometry domain as well as and excavation process and lining installation are summarized in Table 1.

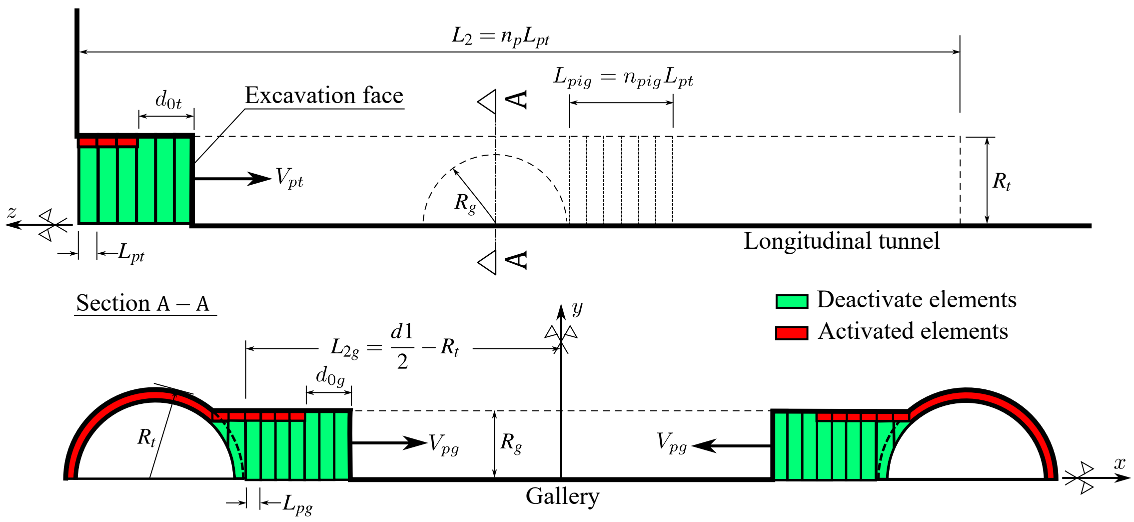

Figure 11: Schematic representation of the excavation process.

Table 1
Parameters related to the geometry of the domain, excavation and installation of the lining.

PARAMETERS	SYMBOL	UNIT	VALUES
Longitudinal tunnels			
Radius of the longitudinal tunnel	R_t	m	R_t
Thickness of the lining	e_t	m	$0.1R_t$
Step length of the excavation process	L_{pt}	m	$1/3R_t$
Unlined length	d_{0t}	m	$2L_{pt}$
Speed of the excavation face	V_{pt}	m/day	12.5
Excavation step time	t_p	day	L_{pt}/V_{pt}
Gallery			
Radius of the gallery	R_g	m	$2/3R_t$
Thickness of the concrete lining	e_g	m	$0.1R_t$
Step length of the excavation process [1]	L_{pg}	m	$1/3R_g$
Unlined length	d_{0g}	m	$2L_{pg}$
Speed of the excavation face	V_{pg}	m/day	12.5
Number of steps that starts gallery excavation	n_{pig}	un	15
Rest of domain			
Distance between longitudinal tunnel axes	d_1	m	$4R_t$ $8R_t$ $16R_t$
Thickness along vertical direction e_y	d_3	m	$20R_t$
Length of the unexcavated region	L_1	m	$10R_t$
Total excavated length	L_2	m	$100L_{pt}$
Thickness along transversal direction e_x	L_3	m	$20R_t + d_1/2$

[1] Value of L_{pg} is slightly different for the last excavation step to match the gallery lengh.

During the tunnel construction phases, the time increment used for the time-dependent analysis is automatically managed by the ANSYS solver. The latter makes use of a semi-implicit scheme for the viscoplasticity solution, together with an automatic time stepping algorithm [39] in which the time step is defined as a fraction of time t_p for the phases of longitudinal tunnel excavation and as a fraction of t_{pg} for the phases of transverse gallery excavation. Furthermore, distinct time steps are considered for the time-dependent analysis during tunnelling process and post-excavation stage. After complete tunnel construction phases, the analysis is carried out for a period of about 3000 days to assess the time evolving deformation as well as long-term viscous effects on the final equilibrium of the tunnel structure. At that respect and in anticipation of the numerical results of the subsequent sections, the characteristic viscoplastic relaxation time [40] is equal to $\bar{\tau} = \eta f_0/E$, which is close to 30 days for model data of Table 2.

6. Preliminary numerical simulations and computational model verification

This section is aimed at applying the computational modeling to simulate deformation and stress in two academic twin tunnels configurations. The numerical results provided in these illustrative applications may be viewed as preliminary verifications of the F.E formulation. The first application refers to unlined twin tunnels excavated in an elastic rock mass, whereas the second application addresses the situation of unlined twin tunnels excavated in an elastoplastic medium.

6.1. Unlined twin tunnels in elastic medium

In the context of plane strain conditions, Guo et al. [9] addressed the configuration of deep twin tunnels excavated in a homogeneous elastic medium in which prevails a hydrostatic initial stress distribution. The authors formulated approximate analytical solutions for the stress distribution establishing far behind the face, which are induced in the rock mass by the excavation of two parallel circular tunnels. The model geometry of the twin circular tunnels as well as loading associated with initial hydrostatic stress (i.e., $\sigma_h = \sigma_v$) are displayed in Fig. 12.

Simulation of the problem has been addressed by means of the 3D finite element model and the numerical results obtained for the stress distribution far behind the faces of the twin tunnel shall be compared to the analytical stress solution derived by Guo et al. [9] in the framework of plane strain conditions. The simulations have been performed taking advantage of symmetry with respect to the midplane between twin tunnels and considering the following model data: tunnel radius $R_t = 4$ m, rock Young modulus $E = 500$ MPa and Poisson ratio $\nu = 0.23$, isotropic initial stresses of $\sigma_v = \sigma_h = 2.2$ MPa.

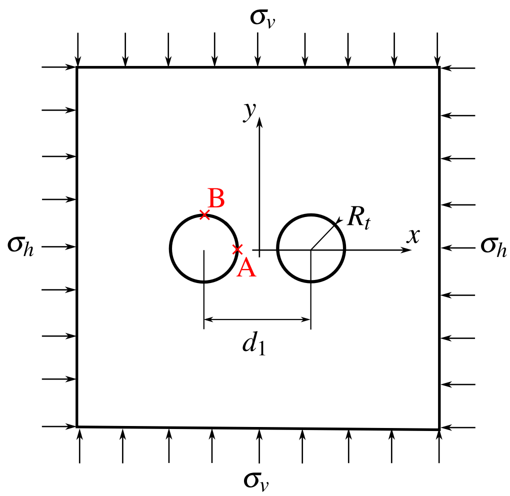

Figure 12: Geometry model and loading mode of the twin circular tunnels studied in Guo et al. [9].

Denoting by u_y the displacement component following the y-axis, Fig. 13 displays the convergence curves $U_B = -u_y(B)/R_t$ that characterize the inward movement at the tunnel roof $B(x = -d_1/2, y = R_t, z)$ as a function of normalized longitudinal distance to the tunnel face. Several values of normalized distances between the twin tunnels axes $d_1/2R_t$ have been investigated, and the configuration of single tunnel may be viewed as the limiting case $d_1/2R_t \gg 1$. It is recalled that in the latter configuration, the convergence far from the tunnel face that is obtained from an elastic analysis reads $U = \sigma_v(1+\nu)/E$. As expected, this figure indicates that the closer the longitudinal tunnels, the greater the convergence at the roof.

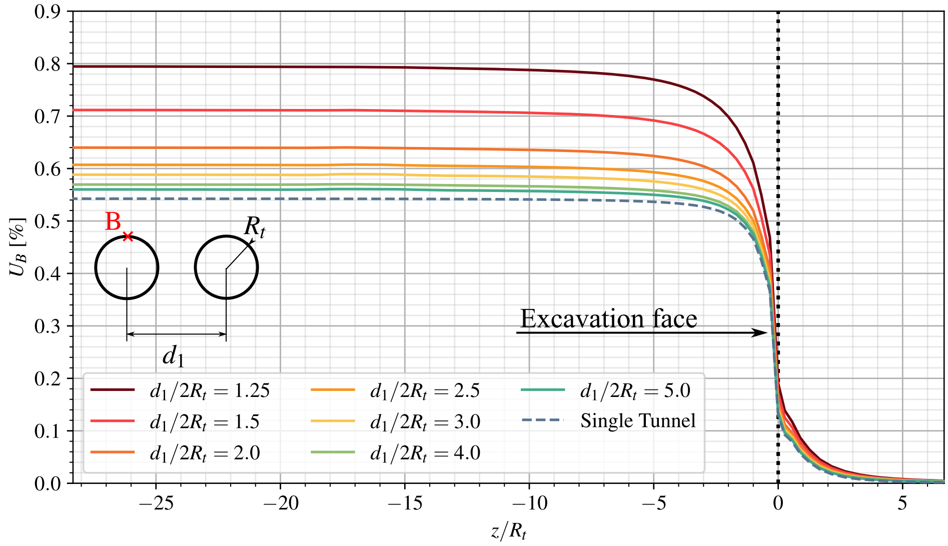

Figure 13: Convergence profiles at the tunnel roof (point B).

The tunnel deformation anisotropy induced by the twin tunnels proximity is illustrated in Fig. 14, which plots the ratio $U_B/U_A = u_y(B)/u_x(A)$ between the vertical displacement u_y at the roof B and the horizontal displacement u_x at the side wall $A(x = -d_1/2 + R_t, y = 0, z)$. The results shown in this figure refer to a tunnel section located far behind the face at normalized distance $z/R_t = -25$. They emphasize the significative tunnel ovalization induced by the proximity of twin tunnel as the distance $d_1/2R_t$ decreases.

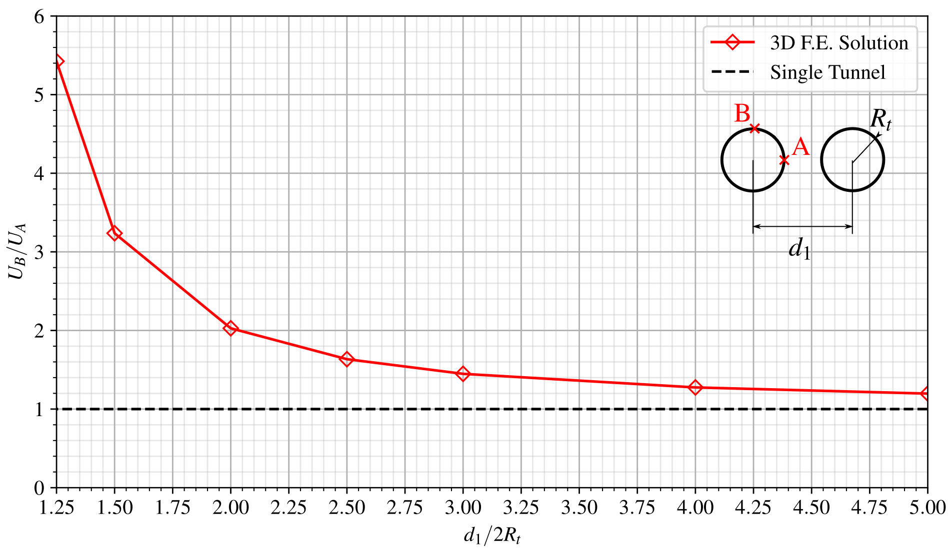

Figure 14: Illustration of the tunnel wall deformation anisotropy induced by twin tunnels proximity.

The stress distribution prevailing far from the tunnel face that were obtained from the 3D numerical simulations are compared in Fig. 15 to the stress solutions derived analytically and numerically in Guo et al. [9]. In this figure, the tangential stress concentration factor σ_{yy}/σ_v computed at the side wall A is plotted for several values of the normalized twin tunnels distance. The results of the theoretical solution to a plate containing two circular holes of equal size presented in Ling et al. [41] are also reported in Fig. 15. It is observed that the results of the 3D finite element simulations correspond to a tunnel section located at normalized distance $z/R_t = -25$ from the face, which is considered sufficient for the plane strain conditions to establish. Interestingly, the tangential stress concentration obtained for a deep single tunnel under plane strain condition simply reads $\sigma_{yy}/\sigma_v = 2$. Although the overall agreement observed between the different predictions, it appears from the comparison that the approximate analytical stress solution provided in [9] slightly overestimates the tangential stress computed at point A as the value of distance $d_1/2R_t$ increases.

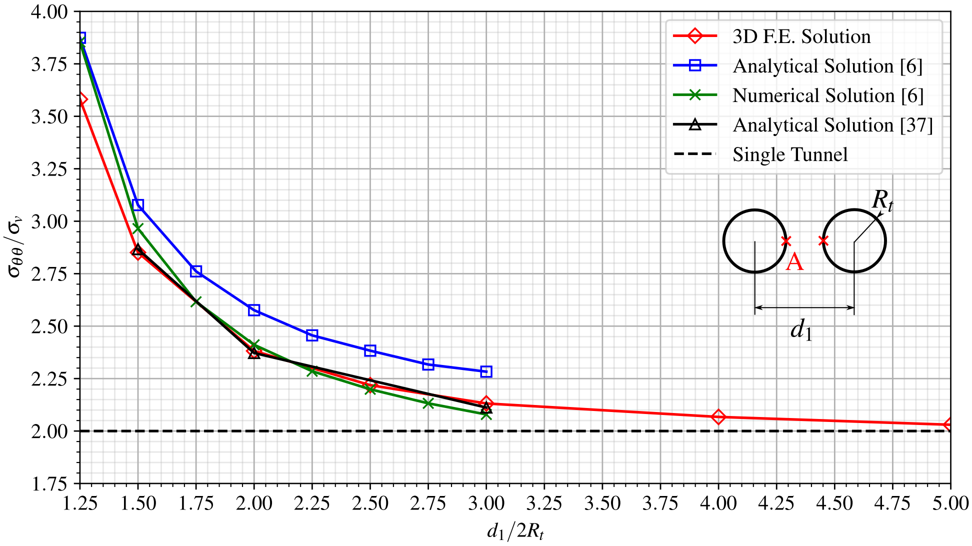

Figure 15: Tangential stress concentration factor at the side wall A versus twin tunnels distance $d_1/2R_t$.

Finally, Fig. 16 displays the distribution of tangential (orthoradial) stress $\sigma_{\theta\theta}$ around the tunnel boundary $\{r = R_t, 0 \leq \theta \leq \pi\}$ considering $d_1/2R_t = 1.5$. The predictions of stress component $\sigma_{\theta\theta}$ obtained from the 3D finite element simulations far behind the tunnel face are shown together with the strain plane solutions derived analytically in [9], emphasizing the ability of the computational model to accurately capture the effect of tunnels proximity on stress distribution.

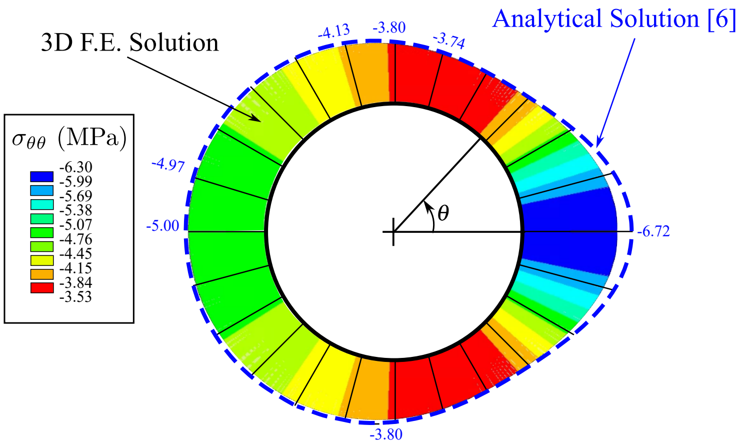

Figure 16: Distribution of tangential stress $\sigma_{\theta\theta}$ around the tunnel wall prevailing far behind the tunnel face (twin tunnels distance $d_1/2R_t = 1.5$).

Keeping in mind it addresses only an academic configuration, the results provided in this section may be viewed as a first preliminary verification of the accuracy of the computational model formulated for the mechanical interaction in deep twin tunnels.

6.2. Unlined twin tunnels in elastoplastic medium

In the analysis developed by Ma et al. [8], an approximate analytical solution has been formulated for the stresses and the plastic zone boundary around deep twin circular tunnels excavated in a homogeneous elastoplastic medium. The approach carried out under the assumption of plane strain condition makes use of the conformal transformation in the complex variable method to transform the solution of the elastic-plastic interfaces into the determination of the mapping function coefficients.

The geometry model and boundary loading conditions associated with the initial stress state are the same as depicted Fig. 12. Unlike the configuration studied in the preceding section, anisotropic initial stress distributions defined by $\sigma_h \neq \sigma_v$ shall be considered in the present analysis. As regards the rock constitutive model, an elastic-perfectly plastic behavior defined by a Mohr-Coulomb criterion with associated plastic flow rule has been adopted in the study. Furthermore, the formulation of stress solution for twin tunnels configuration was based on the premise that the plastic zone around each tunnel completely encloses the tunnel edge and the two plastic zones are not connected.

For the comparison purposes, numerical simulations are carried out by means of the 3D finite element model with the aim to investigate the effect of twin tunnels proximity on the tunnel wall deformation. The following model data has been considered in the F.E simulations: tunnel radius $R_t = 1$ m, rock Young modulus $E = 20$ GPa, Poisson ratio $\nu = 0.3$, friction angle $\phi = 30°$, cohesion $c = 5$ MPa or 2.5 MPa, initial vertical stress $\sigma_v = 30$ MPa or 40 MPa, initial horizontal stress $\sigma_h = 30$ MPa or 40 MPa. The simulation took advantage symmetry with respect to the midplane between the twin tunnels has been used for in the F.E discretization model.

Similarly to the analysis developed in the preceding section, the convergence curves $U_B = -u_y(B)/R_t$, which reflects the inward movement at the tunnel roof $B(x = -d_1/2, y = R_t, z)$, is depicted in Fig. 17 as a function of normalized longitudinal distance to the tunnel face. Several values of normalized distances between the twin tunnels axes $d_1/2R_t$ have been investigated, together with the reference configuration of single tunnel, the latter being viewed as the limiting case $d_1/2R_t \gg 1$. As it could be expected from such simulations, this figure indicates that the proximity of tunnels significantly increases the convergence at the tunnel roof for small values, say $d_1/2R_t < 2$, of twin tunnel spacing. However, this effect rapidly become negligible as soon as the tunnel spacing increases.

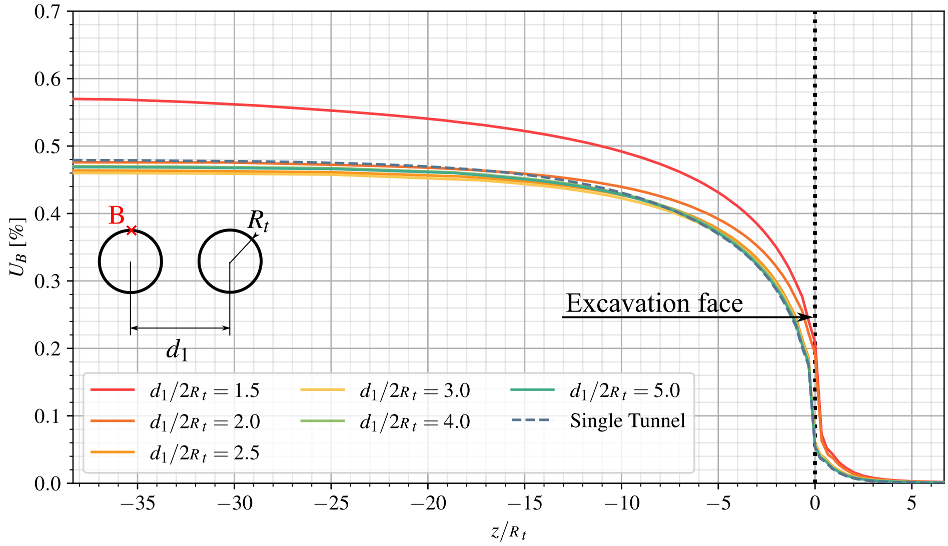

Figure 17: Convergence profiles at the tunnel roof (point B): $c = 5$ MPa, $\sigma_v = \sigma_h = 30$ MPa.

An important feature of the twin tunnels deformation is related to the anisotropy induced by the mutual interaction as the normalized tunnel spacing $d_1/2R_t$ decreases. In that respect, anisotropy of tunnel deformation is illustrated in Fig. 18, which presents the variations of the ratio $U_B/U_A = u_y(B)/u_x(A)$ between the vertical displacement u_y at the roof B and the horizontal displacement u_x at the side wall $A(x = -d_1/2 + R_t, y = 0, z)$ as a function of normalized twin tunnel spacing $d_1/2R_t$. These results refer to a tunnel section located far behind the face at normalized distance $z/R_t = -35$. As observed in the elastic case studied in the preceding section, the proximity of twin tunnels reflected by small values of normalized distance $d_1/2R_t$ is responsible for tunnel ovalization. The magnitude of horizontal displacement at the side wall A is actually larger in than that of vertical displacement at the tunnel roof B, thus indicating an ovalization in the vertical direction (i.e., parallel to y-axis).

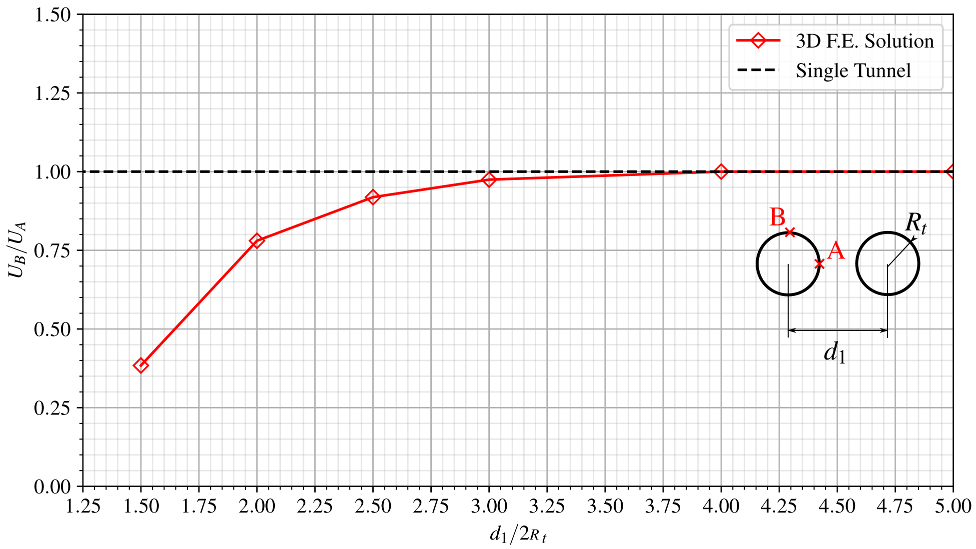

Figure 18: Tunnel wall deformation anisotropy induced by twin tunnels proximity: $c = 5$ MPa, $\sigma_v = \sigma_h = 30$ MPa.

The stress distribution prevailing far from the tunnel face that were obtained from the 3D numerical simulations are compared in the to the approximate stress solutions derived by Ma et al. [8] within the context of plane strain conditions. Fig. 19 displays such a comparison in terms of predicted plastic zone surrounding the twin tunnels considering a normalized tunnel spacing of $d_1/2R_t = 2.5$. Different values have been considered for rock cohesion c and initial stresses σ_v and σ_h. It appears from the latter figure that the finite element modeling produces predictions very similar to those provided in 19. The results also illustrate that larger plastic zones arise when the cohesion c is smaller.

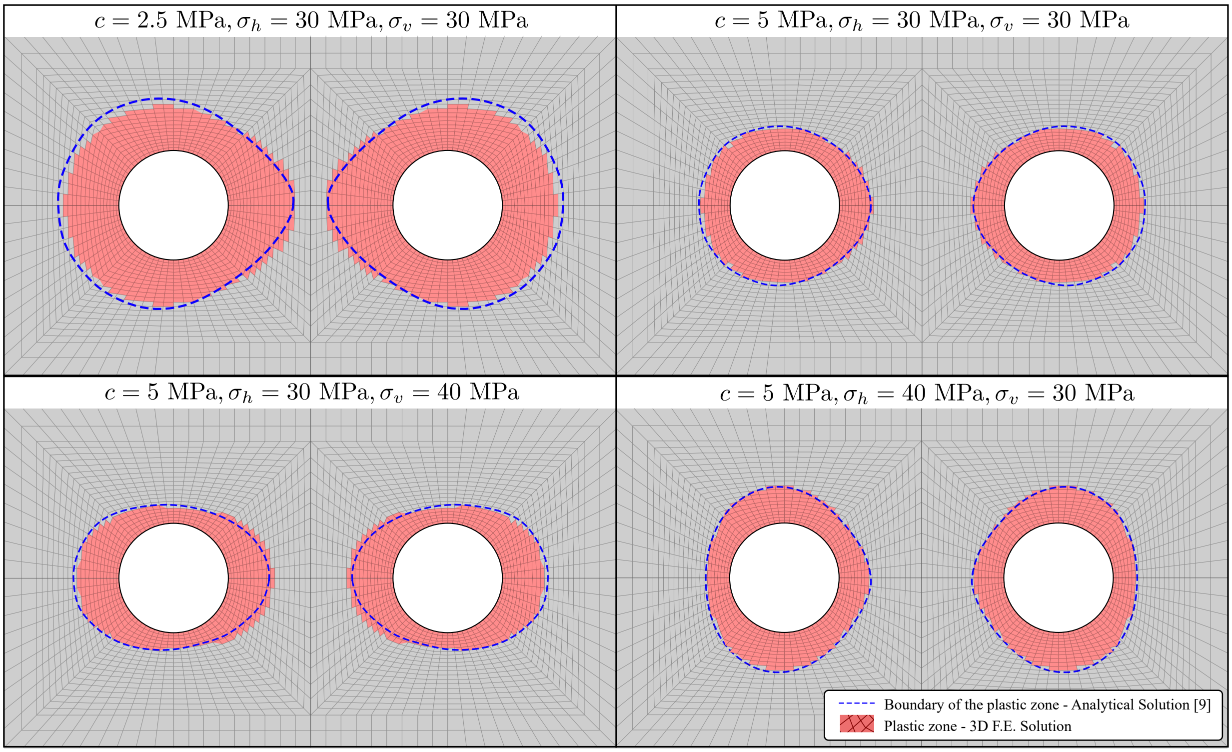

Figure 19: The plastic zone extent obtained from the present F.E. simulations and from the stress solution provided in [8].

Further comparisons are shown in Fig. 20, which presents the plots of radial σ_{rr}, and orthoradial $\sigma_{\theta\theta}$ stress components along three radial paths defined in polar coordinates by $\theta = 45°, 90°$ and $135°$. It should be pointed out that, although the F.E element simulations make use of the Drucker-Prager yield surface inscribed to the Mohr-Coulomb one (used in the solution of Ma et al. 8), the numerical predictions are matching well with the analytical stress solution.

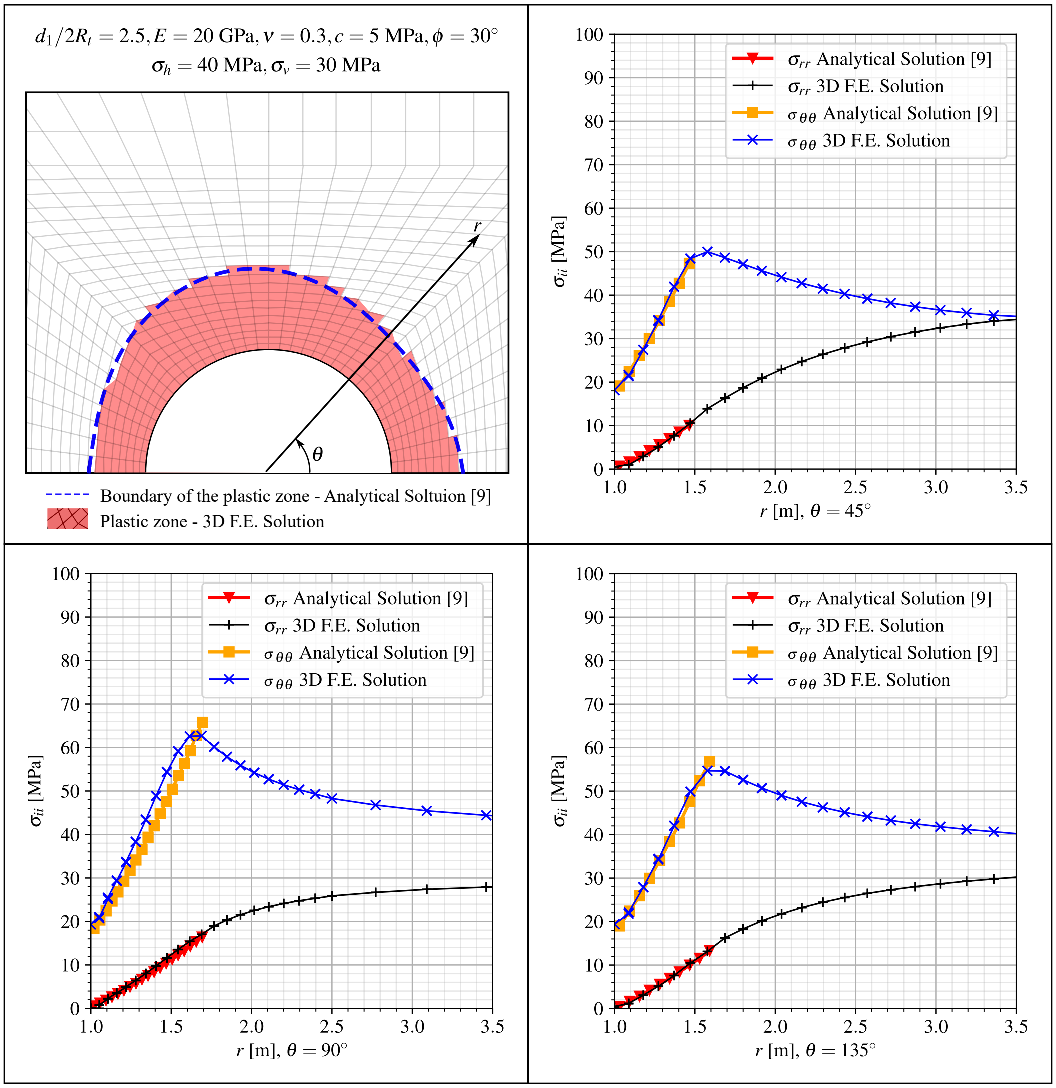

Figure 20: Distribution of radial and orthoradial stress components along different radial directions: comparison between numerical and analytical predictions.

7. Three-dimensional finite element simulations

This section provides some numerical results related to rock deformation in twin tunnels with transverse gallery obtained from the 3D computational model presented in sections 3, 4 and 5. It is emphasized that the primary objective herein is to illustrate the capabilities of the proposed formulation to address within a 3D context the configuration of a complex tunnel structure involving nonlinear and time-dependent couplings. Elaboration of an exhaustive parametric analysis integrating the effects of geometrical, constitutive and loading parameters is notably beyond the scope of the numerical application.

7.1. Model data and preliminary considerations

The rock constitutive data used in the subsequent analysis refer to a deep clay from eastern Paris basin (Aisne region, France) studied in [23, 25, 27, 42]. The material properties including elastoplastic and viscoplastic parameters summarized in Table 2 have been evaluated and calibrated from an extensive series of laboratory tests performed under undrained conditions [23, 27, 42]. The Aisne clay rocks exhibit high density (2.01 to 2.57 g/cm^3), a low average water content (between 3 to 11%) and relatively low porosity (typically less than 20%). It is therefore assumed that hydromechanical coupling can be neglected in the analysis of rock material deformation. In particular, the creep tests indicated that the long-term effects primarily stem from material viscosity, with a very low proportion induced by pore pressure redistribution. An important characteristic of the behavior such clay is that irreversible strains are observed in cyclic tests even at small values of axial strain (less than 0.3%). The instantaneous undrained triaxial tests performed at high confining pressure values, such as those prevailing in the rock mass at approximately 450 m deep, indicated that the maximum deviatoric stress remains approximately constant, thus suggesting a Tresca-type failure criterion for the short-term component of the behavior. As for the long-term behavior, the creep tests revealed that the deviatoric stress threshold beyond which the material exhibits creep deformation is almost independent on the mean stress, suggesting that the time-dependent behavior component can be conveniently described by a Tresca-like criterion. Comparison of instantaneous and delayed behaviors reveals that short-term cohesion exceeds long-term cohesion within a ratio ranging between 1.2 and 2. Based on these observations, the constitutive model data adopted for the elastoplastic and viscoplastic components of rock material behavior is summarized in Table 2.

Table 2 also presents the constitutive parameters used for the lining used for the twin tunnels and gallery, the instantaneous relaxation modulus under uniaxial stress at 28 days being referred to as $E_{c_{28}}$. In the analyses that considers elastic behavior of the lining, the concrete elastic modulus is set equal to $E_{c_{28}}$. When viscoelastic behavior is adopted for the lining, the relaxation modulus evolves in time according to the Generalized Kelvin model described in section 4, whereas the Poisson ratio is assumed to be constant within the time interval of analysis. During the tunnel construction process, loading and creep of each lining segment starts from the moment it is activated with properties at age $t_0 = 1$ day, whereas shrinkage effects are assumed to take part at the age of $t_s = 7$ days.

Table 2
Constitutive parameters used in the numerical analysis.

PARAMETERS	SYMBOL	UNIT	VALUES
Constitutive model of rock mass			
Young's modulus	E	MPa	1500
Poisson's ratio	ν	-	0.49
Plastic cohesion	c	MPa	$4\sqrt{3}/2$
Plastic friction angle	ϕ	°	0
Viscoplastic cohesion	c_{vp}	MPa	$2\sqrt{3}/2$
Viscoplastic friction angle	ϕ_{vp}	°	0
Power law parameter	n	-	1
Reference parameter	f_0	MPa	1
Viscosity coefficient	η	day	40000
Constitutive model of lining			
Characteristic compressive strength at age of 28 days	f_{ck}	MPa	20
Modulus of elasticity at the age of 28 days	$E_{c_{28}}$	MPa	30303
Poisson's ratio	ν_c	-	0.2
Coefficient defining instantaneous relaxation modulus [32]	s	-	0.2
Relative humidity of ambient environment	RH	%	70
Notional size of member - longitudinal concrete lining	h_t	cm	0.2111
Notional size of member - gallery concrete lining	h_g	cm	0.2176
Age of concrete at the beginning of shrinkage	t_s	days	7
Shrinkage coefficient depending on cement type [32]	β_{sc}	-	8
Temperature	T	°C	20
Age of concrete at loading	t_0	days	1

The parameters defining the structure geometry as well as the excavation and lining installation process are provided in Table 1. All the length parameters are normalized by the tunnel radius R_t, which amounts to formally consider radius $R_t = 1$ m in the numerical simulations. As mentioned in Table 1, three different values shall be considered in the simulations for the distance between twin tunnels axes, namely $d_1 = 4R_t$, $d_1 = 8R_t$, and $d_1 = 16R_t$. In addition, constant values of tunnel and gallery advancement rates are considered and fixed to $V_{pt} = V_{pg} = 12.5$ m/day. As regards the initial stress state prevailing prior to excavation processes, hydrostatic stress distribution with $\sigma_v = \sigma_h = 9$MPa, corresponding to geostatic conditions at depths of about of 450 m, is adopted in the subsequent simulations.

The numerical study investigates the long-term and short-term tunnel convergence profiles considering various constitutive models for the rock mass (elastic, elastoplastic, viscoplastic or elastoplastic-viscoplastic) and for the lining (elastic and viscoelastic). For the comparison purposes, the configuration of unlined tunnel as well as the configurations with or without transverse gallery will also be analyzed. To facilitate the description of the different configurations addressed below, Table 3 provides the list of each configuration as well as associated abbreviation used to refer to in the presentation of numerical results.

Table 3
Configurations and associated abbreviations used in numerical simulations.

DESCRIPTION	ABBREVIATION
Elastic rock mass	E
Elastoplastic rock mass	EP
Elastoviscoplastic rock mass	VP
Elastoplastic-Viscoplastic rock mass	EPVP
No lining	NL
Elastic lining	EL
Viscoelastic lining	VEL
Long-term	LT
End of excavation process (Short-term)	ST
With Gallery	WG
No Gallery	NG

Denoting by u_y the displacement component along the vertical y-axis, all the results presented in the following analyses will specifically refer the convergence profile $U_B = -u_y(B)/R_t$ that characterizes the inward movement of the tunnel roof $B(x = -d_1/2, y = R_t, z)$ as a function of the normalized algebraic longitudinal distance z/R_t from the excavation face. In addition, point $C(x = -d_1/2, y = R_t, z = -25R_t)$ has been chosen as representative of the equilibrium convergence U_C far behind the tunnel face and transverse gallery. When the gallery intersects the longitudinal tunnel, the highest convergence value U_{peak} highlighted in the plots of convergence curves refers to point $D(x = -d_1/2, y = R_t, z = L_1 + L_2/2)$ located at the roof of longitudinal tunnel section lying at the tunnel/transverse gallery junction.

The first feature of tunnel deformation to be mentioned is related to the tunnel deformation anisotropy (or ovalization) induced by the twin tunnels proximity. A single circular tunnel excavated in a homogeneous isotropic rock mass with hydrostatic initial stress state will deform symmetrically so that the circular shape of tunnel wall will be preserved throughout the excavation process. As already pointed out in the preliminary numerical simulations presented in section 6, the mutual interaction associated with twin tunnels proximity will in contrast result in anisotropic deformation of the tunnel wall, the ovalization effect being more pronounced as the distance between twin tunnels axes d_1 decreases. For illustrative purposes, Fig. 21 presents schematic plots of the deformed tunnel wall far behind the face together with trajectory of monitoring point B considering three different values of normalized twin tunnel spacing d_1/R_t. The configuration shown in this figure corresponds to elastoplastic rock mass (EP), elastic lining (EL) and transverse gallery (WG). It should be however kept in mind that due to tunnel ovalization, U_B would not be therefore sufficient for characterizing the whole deformation of the tunnel wall.

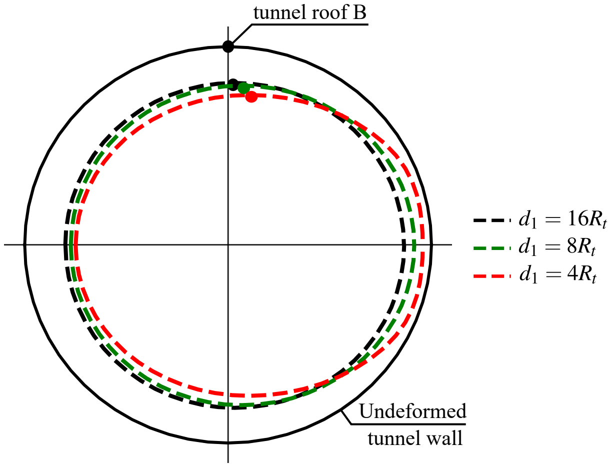

Figure 21: Illustration of the deformation anisotropy induced by twin tunnels proximity.

The second feature of the tunnel deformation that deserves to be mentioned refer the specific deformation patterns prevailing in the region surrounding the tunnel wall. In consistence with experimental data, the plastic cohesion c and viscoplastic cohesion c_{vp} reported in Table 2 comply with condition $c > c_{vp}$. This notably implies that irreversible viscoplastic strains will be activated earlier as the tunnel excavation. Schematic representation of deformation patterns within the rock mass is illustrated in Fig. 22.

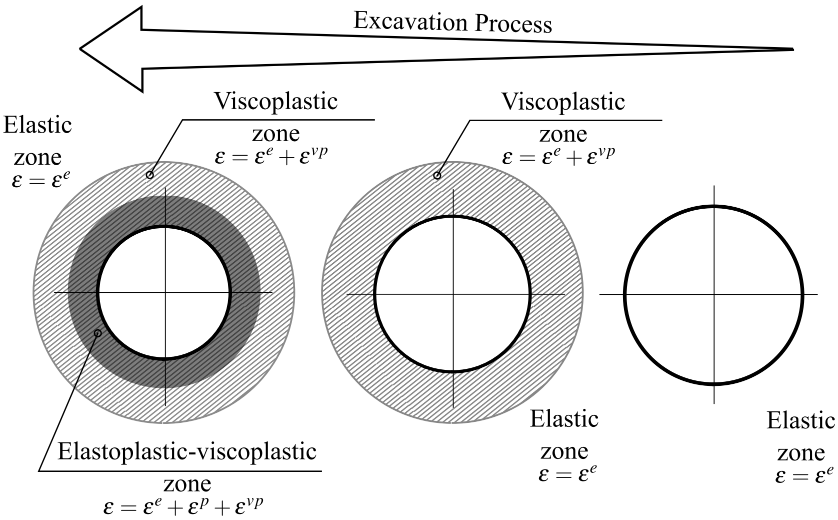

Figure 22: Evolution of deformation zones as the tunnel excavation proceeds.

[parei aqui]

7.2. Short and long-term convergence profiles

Figs. 23, 24, and 25 show the convergence profiles in the twin tunnels with gallery (WG) considering the different constitutive models of the rock mass (E - blue, EP - yellow, VP - magenta, EPVP - red and green) and of the lining (EL and VEL). The interaction effect rising from twin tunnels proximity is investigated by considering three values $d_1 = 4R_t$, $d_1 = 8R_t$, and $d_1 = 16R_t$. The solid lines refer to short-term analysis (ST) whereas the dashed lines to long-term analysis (LT).

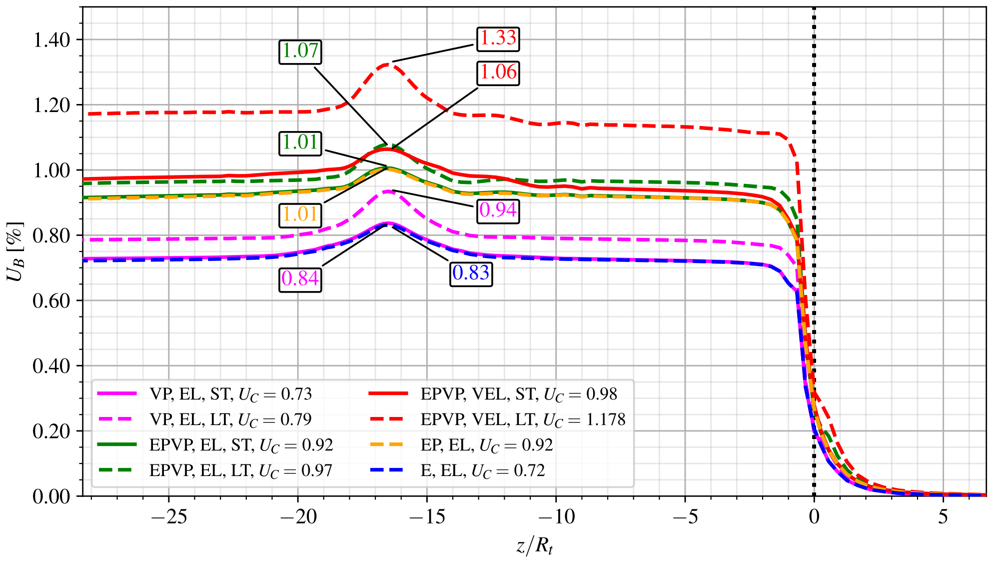

Figure 23: Convergence Profiles: short-term (ST) and long-term (LT) analyses for the configuration with gallery (WG) and distance between twin tunnels $d_1 = 16R_t$.

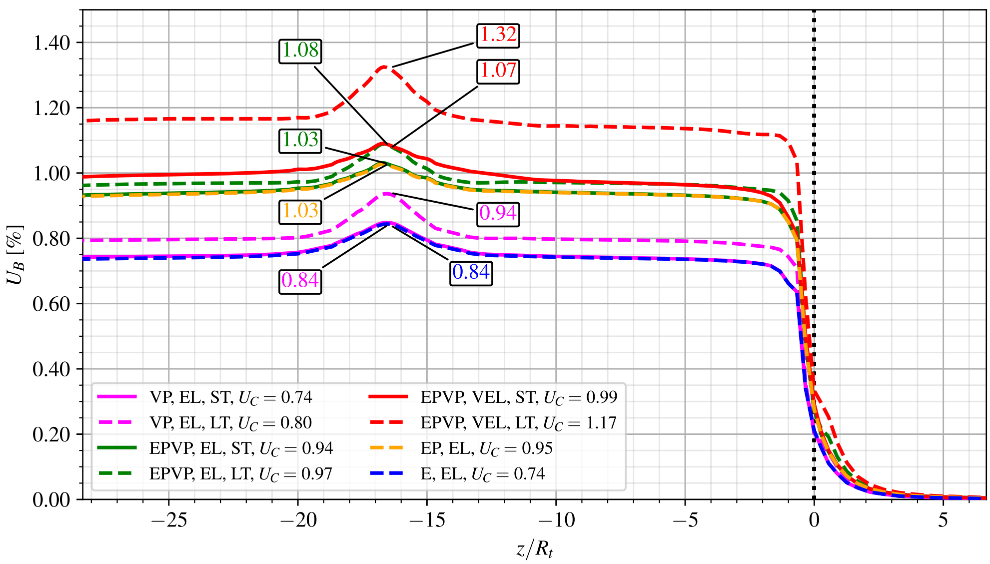

Figure 24: Convergence Profiles: short-term (ST) and long-term (LT) analyses for the configuration with gallery (WG) and distance between twin tunnels $d_1 = 8R_t$.

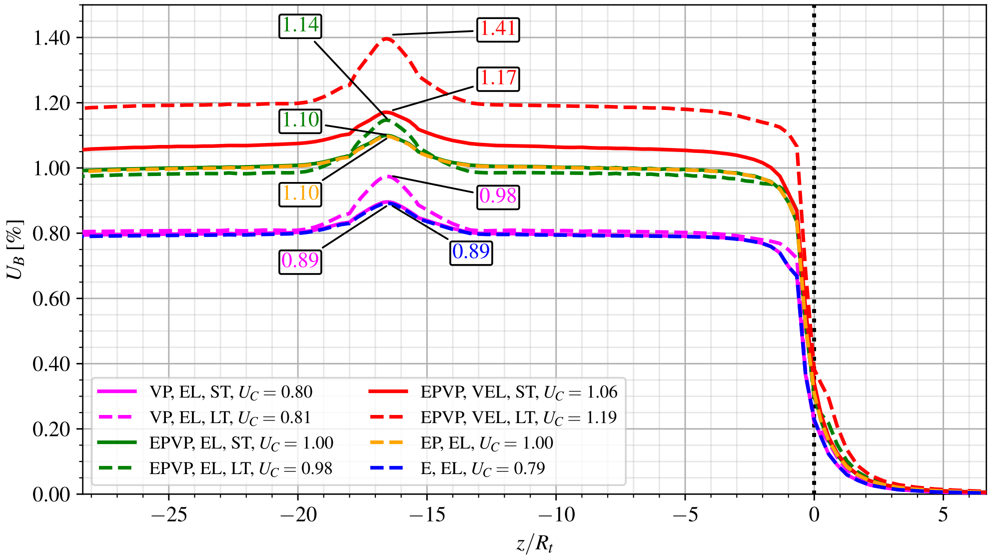

Figure 25: Convergence Profiles: short-term (ST) and long-term (LT) analyses for the configuration with gallery (WG) and distance between twin tunnels $d_1 = 4R_t$.

For all investigated values of twin tunnels distance d_1, the convergence profiles obtained in short-term (ST) analyses are very similar for both the E-EL (blue dashed line) and the VP-EL (magenta solid line) constitutive model configurations. This mainly attributed to relatively high value considered for the tunnel/gallery advancement rate and lining installation (excavation speed $V_{pt} = V_{pg}$), thus limiting the viscous effects on the tunnel deformation. The same explanation holds regarding the results derived from the short-term (ST) analyses with the EP-EL (yellow dashed line) or EPVP-EL (green solid line) constitutive model configurations. However, the viscous effects give rise to delayed tunnel deformation progressively affecting the long-term (LT) convergence (dashed green line) at the tunnel roof B. The discrepancy between short-term and long-term responses is more pronounced when a time-dependent viscoelastic lining is considered, as clearly indicated from the convergence associated with the EPVP-VEL model (solid and dashed red lines).

It is noted that the relatively high stiffness considered of the elastic lining is likely to significantly reduces the viscous component of tunnel wall deformation. This can be illustrated by analyzing the short-term and long-term convergences for VP-EL model (solid and dashed magenta line). In this configuration, the twin tunnels proximity induces a substantial increase in the short-term (ST) prediction of U_C when comparing $d_1 = 8R_t$ and $d_1 = 4R_t$, whereas the long-term (LT) convergence hardly changes mainly due to the restriction imposed by the stiff lining.

Referring to the configuration analyzed in Figs. 23, 24, and 25, the ovalization effect may be illustrated by visualizing in Fig.Fig. 26 the anisotropic deformation of a tunnel cross-section located far behind the face in the particular case of twin tunnel distance $d_1 = 4R_t$. In this figure, the configuration of a single circular tunnel ($d_1 \to \infty$) is also shown as a reference case.

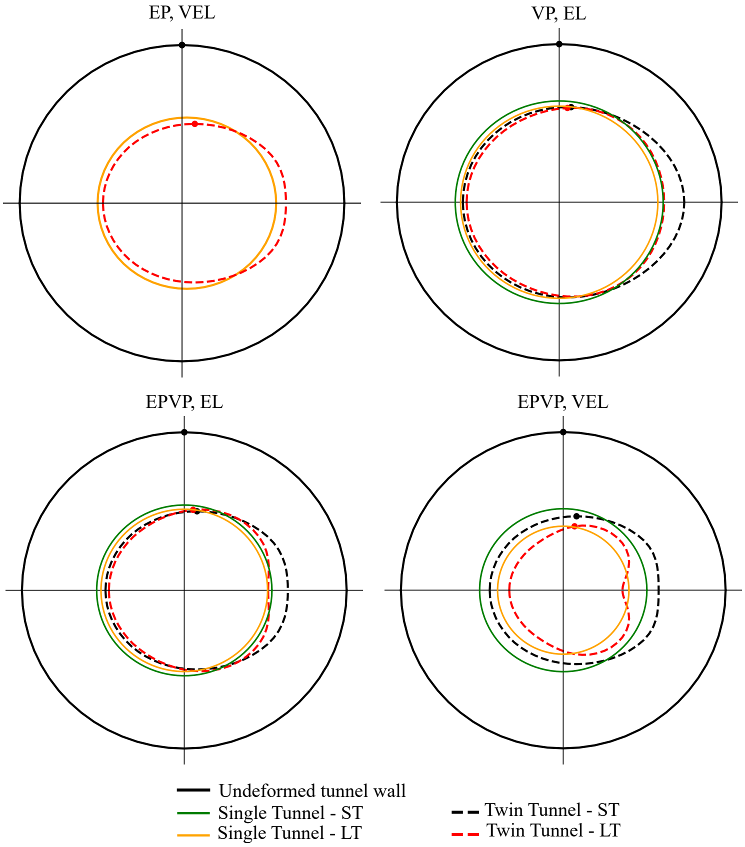

Figure 26: Illustration of deformation anisotropy induced: configuration with gallery (WG) and distance between twin tunnels $d_1 = 4R_t$.

In that respect, Fig. 27 provides further illustration of the ovalization effect by plotting the anisotropy ratio $U_B/U_A = u_y(B)/u_x(A)$ between the vertical displacement u_y at the roof B and the horizontal displacement u_x at the side wall $A(x = R_t - d_1/2, y = R_t, z)$. The resulted presented in this figure correspond to twin tunnels without transverse gallery (NG) and distance $d_1 = 4R_t$. The results suggest a more pronounced ovalization effect short-term tunnel deformation (solid lines).

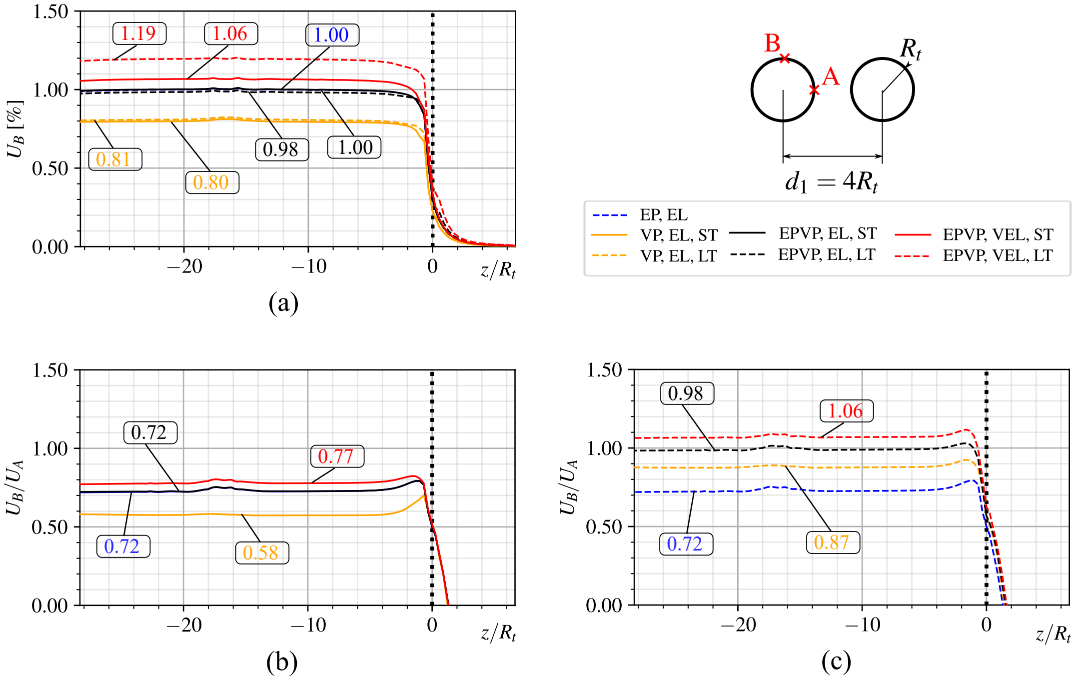

Figure 27: Deformation anisotropy induced by twin tunnels proximity for the configuration without gallery (NG) and distance between twin tunnels $d_1 = 4R_t$: (a) convergence profile at the tunnel roof B, (b) anisotropy ratio obtained in short-term analysis, (c) anisotropy ratio obtained in long-term analysis.

7.3. Additional numerical analysis: impact of creep deformation

This section provides further numerical results obtained from long-term and short-term analyses, with particular emphasis on the effect of time-dependent behavior of the rock material and lining constituent materials. Fig. 28 displays the long-term convergence profiles for $d_1 = 16R_t$, $8R_t$ and $4R_t$ (yellow, green and red lines, respectively) considering viscous constitutive models: viscoplastic rock mass with elastic lining (VP-EL - solid lines), elastoplastic-viscoplastic rock mass with elastic lining (EPVP-EL - dashed line) and viscoelastic lining (EPVP-VEL - dotted lines). To emphasize the interaction rising from twin tunnels proximity and transverse gallery, the results obtained in the reference configuration of a single tunnel (black lines) are also shown. Close values of the peak convergence U_{peak} are obtained at the tunnel roof for the EPVP-VEL model with $d_1 = 16R_t$ (yellow dotted line) and with $d_1 = 8R_t$ (green dotted line). This result may be explained by the fact the overall interaction effect on tunnel convergence results from the competing effects of twin tunnel proximity (defined by d_1) and the time necessary for complete gallery excavation and its intersection with longitudinal tunnel (also defined by length by d_1). The results indicated that these competing phenomena lead to equivalent overall effect in the cases of $d_1 = 8R_t$ and $d_1 = 16R_t$. In the case of $d_1 = 4R_t$ (red dotted line), the effect of twin tunnel proximity appears to be predominant, which lead to higher value of the peak convergence U_{peak}.

Referring to EPVP-VEL and EPVP-EL models (dotted lines and dashed lines), it can be seen from the results of Fig. 28 that higher convergence values are associated with time-dependent behavior of the lining. Unlike the stiff elastic lining, the aging viscoelastic lining induces evolving tunnel convergence along the excavation process.

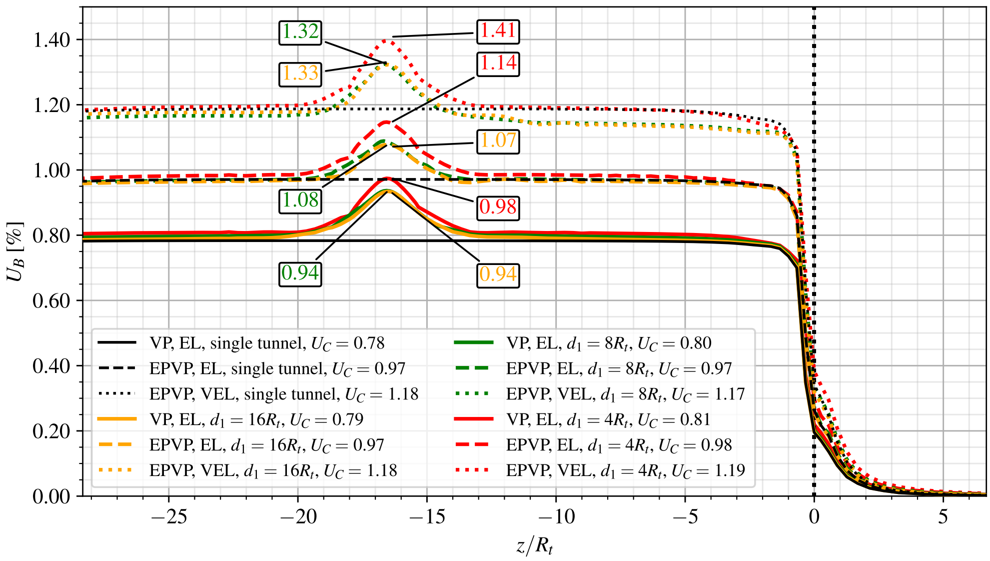

Figure 28: Long-term convergence profiles for the configuration of twin tunnels with transverse gallery (WG): effect of rock mass and lining creep deformation.

The impact of creep deformation on the tunnel convergence can alternatively be illustrated based on the comparison of the numerical predictions obtained in the cases of instantaneous behavior (elastoplastic, elastic) and time-dependent behavior (viscoplastic, viscoelastic) for the constituent materials. Fig. 29 depicts the convergence profiles obtained for $d_1 = 16R_t$, $8R_t$ and $4R_t$ (yellow, green and red lines, respectively) considering the configurations of elastoplastic rock mass with elastic lining (EP-EL - solid lines), elastoplastic-viscoplastic rock mass with viscoelastic lining in short-term analysis (EPVP-VEL-ST - dotted lines) and elastoplastic-viscoplastic rock mass with viscoelastic lining in long-term analysis (EPVP-VEL-LT - dashed lines). The case of single circular tunnel ($d_1 \to \infty$) is also analyzed as reference configuration (black lines).

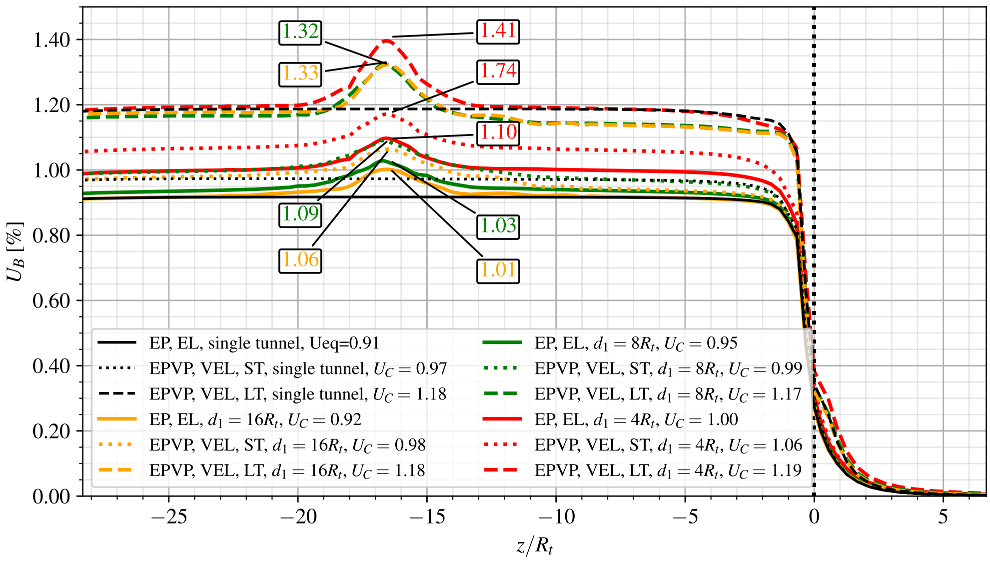

Figure 29: Short-term and long-term convergence profiles obtained for the configuration of twin tunnels with transverse gallery (WG): instantaneous versus delayed behaviors of the rock and lining constituent material.

Once again, the result predictions shown in this figure emphasize the significative impact of the viscoelastic lining behavior on the short-term convergence profile of the tunnels. At short-term (ST), the elastoplastic-viscoplastic rock mass with viscoelastic lining (EPVP-VEL - dotted lines) leads to higher convergences when compared to the elastoplastic rock mass with elastic lining (EP-EL - solid lines). This is mainly attributed to the fact the early age viscoelastic lining (VEL) exhibits lower relaxation modulus than the stiffness $E_{c_{28}}$ considered for elastic lining (EL), thus resulting in higher tunnel deformation. Regarding the long-term analysis (LT), even though the viscoelastic lining (VEL) (dashed lines) exhibit increasing relaxation modulus due to aging phenomenon, the creep deformation of both the rock and lining constituents result in significantly higher convergences at the tunnel roof when compared to obtained for elastoplastic rock with elastic lining (EP-EL - solid lines). A noticeable increase in the magnitude of U_{peak}, induced by the interaction with transverse gallery, is also observed from the short-term response (dotted lines) to the long-term response (dashed lines), highlighting once again the influence of the delayed behavior of the rock and the lining.

7.4. Effect of the lining stiffness on the tunnel convergence

In tunnel deformation analyses, the behavior of the concrete lining is classically characterized by the elastic stiffness parameter, which relates the normal stress exerted by the surrounding the rock mass and the normalized lining normal displacement (convergence). The elastic the elastic stiffness parameter is computed from the elastic properties of concrete material and the lining thickness (normalized by the tunnel radius) [43, 44]. This concept is extended herein to case of viscoelastic lining by in traducing the instantaneous stiffness modulus at 28 days $K_{c_{28}}$ as:

$$K_{c_{28}} = \frac{E_{c_{28}}}{1+\nu_c} \frac{1-(1-e_t/R_t)^2}{(1-2\nu_c)+(1-e_t/R_t)^2} \tag{12}$$

In the above analyses of sections 7.1, 7.2 and 7.3 the lining thickness were fixed to $e_t = e_g = 0.1R_t$, corresponding to lining stiffness $K_{c_{28}} = 3400$ MPa. As far as the tunnel deformation is concerned, the latter value characterizes a rather stiff lining, which might be a predominating factor for the control of tunnel convergence.

To assess the effect of the lining stiffness on the convergence profile, a smaller value $e_t = e_g = 0.03R_t$, corresponding to lining stiffness modulus $K_{c_{28}} = 970$ MPa, will be in the numerical simulations. Referring to the particular case of a rock mass exhibiting elastoplastic behavior (EP), that is only instantaneous behavior, Fig. 30 and

Fig. 31 display the convergence profiles at tunnel roof predicted respectively for $d_1 = 16R_t$ and $d_1 = 4R_t$. Three configurations for the support lining are considered: unlined structure (NL - dashed lines), elastic lining with lower stiffness $K_{c_{28}} = 970$ - dotted lines), and elastic lining with higher stiffness $K_{c_{28}} = 3400$ - solid lines). In addition, the numerical simulations include the cases with transverse gallery (WG - blue lines) and without gallery (NG - yellow lines). The reference configuration of a single tunnel is also studied (black lines).

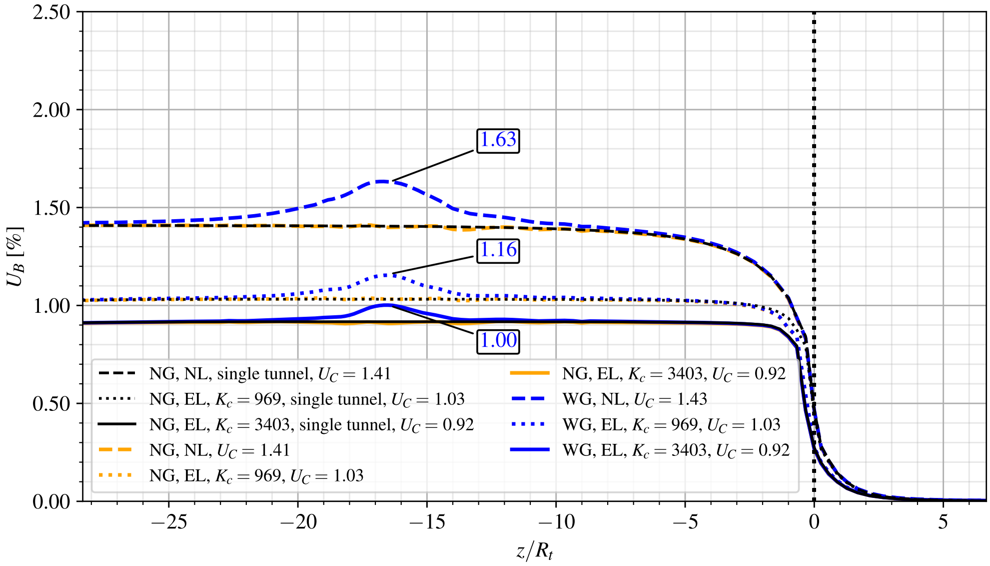

Figure 30: Effect of lining stiffness on the convergence profiles for the configuration of twin tunnels with and without transverse gallery and distance between twin tunnels $d_1 = 16R_t$ - elastoplastic rock mass, without and with elastic lining.

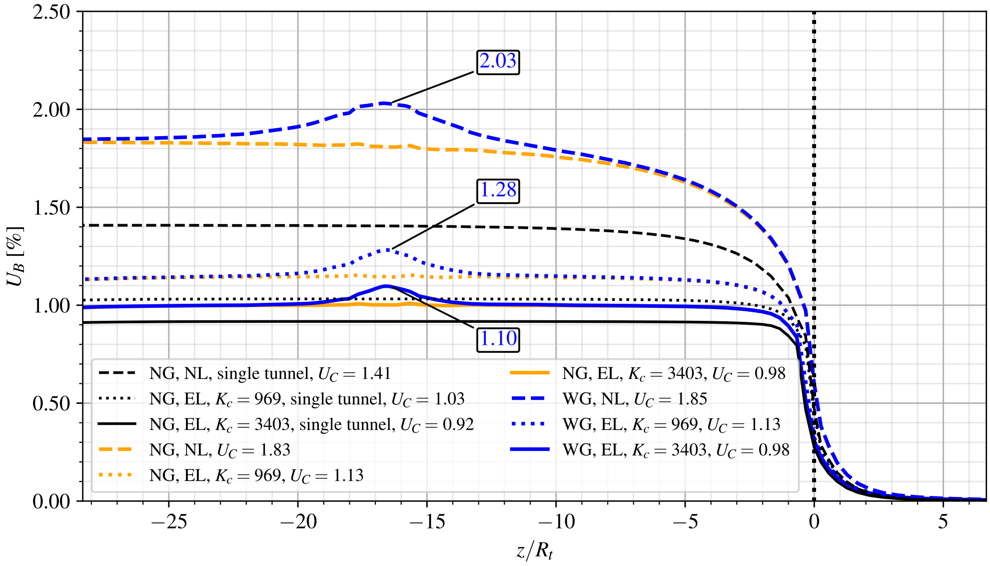

Figure 31: Effect of lining stiffness on the convergence profiles for the configuration of twin tunnels with and without transverse gallery and distance between twin tunnels $d_1 = 4R_t$ - elastoplastic rock mass, without and with elastic lining.

As observed in the simulations of preceding sections, the equilibrium convergence U_C far behind the tunnel face is almost unaffected by the presence of transverse gallery.

Regarding first the effect of lining stiffness on the convergence of single tunnel, the stiffer lining (black solid line) leads to a stabilized convergence reduction of approximately 35% with respect to unlined structure (black dashed line), whereas this reduction is only 12% for the moderate stiffness lining (black dotted line).

For twin tunnels with spacing $d_1 = 16R_t$, the predictions of stabilized convergence U_C (blue and yellow lines) provided in Fig. 30 are close for each lining configuration to those obtained for a single tunnel (black lines). In contrast, the interaction between the twin tunnels reveals significative when the spacing reduces to $d_1 = 4R_t$. In that case, the combined impact of lining support and twin tunnels proximity can be assessed by comparing in Fig. 31 the values of convergence U_C predicted for $d_1 = 4R_t$ (yellow and blue solid lines) and $d_1 \to \infty$ (single tunnel - black lines). Compared to the convergence of single tunnel, the increase in convergence induced by twin tunnels proximity reaches values of 30% for unlined structure, 10% for the moderate stiffness lining and 6.5% for the higher stiffness stiff.

Analyzing the effect of lining stiffness on the disturbed region associated along the convergence profile with the presence of transverse gallery, it is first observed that the increase in stiffness reduces in all studied configurations the extent of the disturbed region, whereas the twin tunnels spacing has little impact. For the configuration of spacing $d_1 = 16R_t$, where the interaction due to twin tunnels proximity is expected to be minor, the ratio $(U_{peak} - U_C)/(U_C)$ defining the relative variation between peak value and stabilized tunnel roof convergence is about 14% , 12.5% and 8.7% according to the lining stiffness value: $K_{c_{28}} = 0$ (unlined), $K_{c_{28}} = 970$ MPa and $K_{c_{28}} = 3400$ MPa. The values of this ratio are altered to about 9.7%, 13% and 12% for the configuration with spacing $d_1 = 4R_t$ in which both effects of lining stiffness and tunnels proximity are simultaneously acting.

In line with the previous analysis investigating the impact of instantaneous stiffness modulus $K_{c_{28}}$ of the lining, Fig. 32 and Fig. 33 present the long-term convergence results in the configurations of elastoplastic-viscoplastic rock mass (EPVP) and viscoelastic lining (VEL) with gallery (WG - blue lines) and without gallery (NG - yellow lines), considering twin tunnels spacing $d_1 = 16R_t$ and $4R_t$, respectively. The results obtained for the reference single tunnel configuration are also provided (black lines).

Similar to the previous analysis involving constituent materials that exhibit only instantaneous behaviors, the results Fig. 32 indicate that the predictions of stabilized convergence U_C in the case of twin tunnels with spacing $d_1 = 16R_t$ are very close to obtained for single tunnel.

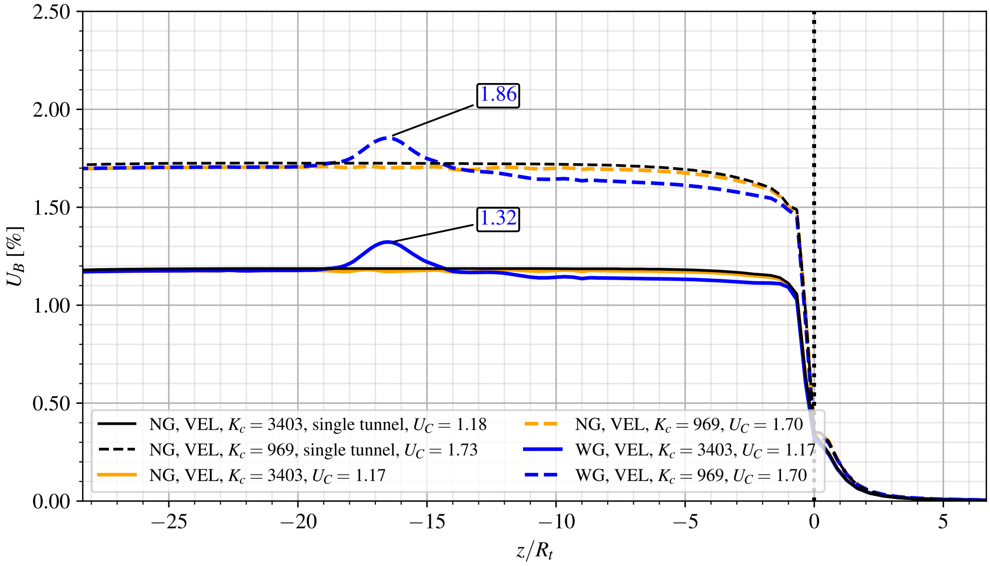

Figure 32: Effect of instantaneous lining stiffness on the long-term convergence profiles for the configuration of twin tunnels with and without transverse gallery and distance between twin tunnels $d_1 = 16R_t$ - elastoplastic-viscoplastic rock mass, without and with viscoelastic elastic lining.

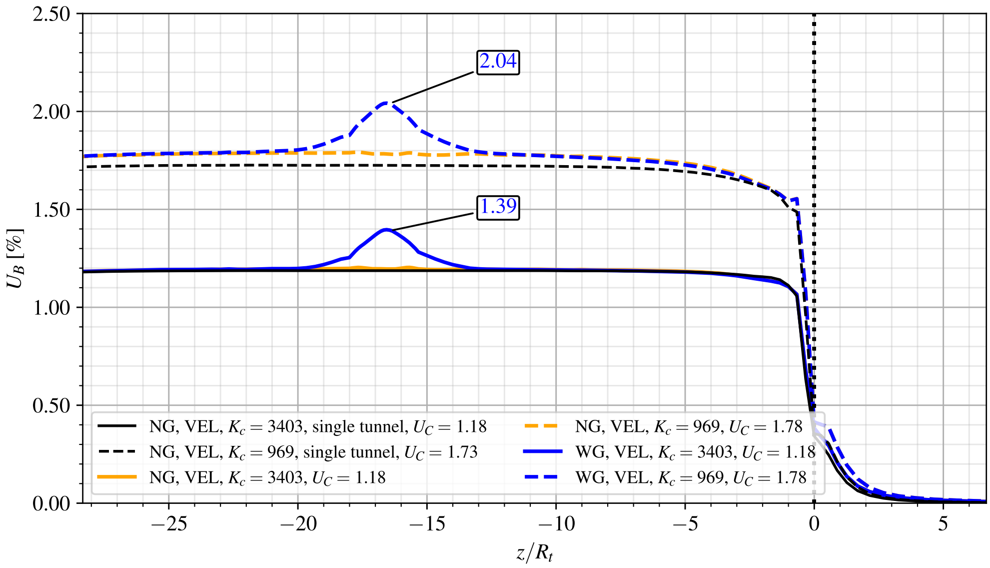

Figure 33: Effect of instantaneous lining stiffness on the long-term convergence profiles for the configuration of twin tunnels with and without transverse gallery and distance between twin tunnels $d_1 = 4R_t$ - elastoplastic-viscoplastic rock mass, without and with viscoelastic elastic lining.

Even in the specific case of $d_1 = 4R_t$ where a strong twin tunnels interaction would be expected, the role of lining with higher stiffness on stabilized convergence (blue and yellow solid lines in Fig. 33) is predominating with values close to obtained for single tunnel (black solid line in Fig. 33), thus masking such interaction effect. For lower lining stiffness, the numerical results (blue and yellow dashed lines) indicate a small increase in the value of U_C when compared to the single tunnel (black dashed line).

As regards the impact on the peak convergence U_{peak} and extent of the gallery influence zone (disturbed portion of convergence profile), the results show that for each value of twin tunnels spacing d_1, the latter extent is slightly affected by the instantaneous lining stiffness modulus. In contrast the ratio U_{peak}/U_C is significantly affected by the values of d_1 and $K_{c_{28}}$. For the configuration with $d_1 = 4R_t$, it respectively takes the values U_{peak}/U_C =14.5% and 18% lower and higher lining stiffness, whereas it respectively takes the values 9.5% and 13% for the configuration with $d_1 = 16R_t$.

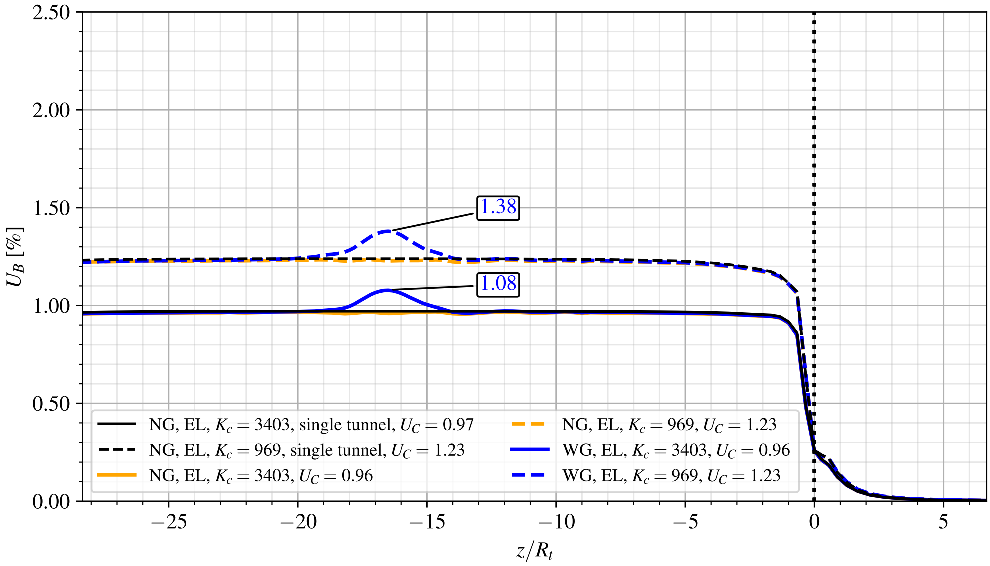

Figure 34: Effect of lining stiffness on the long-term convergence profiles for the configuration of twin tunnels with and without transverse gallery and distance between twin tunnels $d_1 = 16R_t$ - elastoplastic-viscoplastic rock mass, without and with elastic lining.

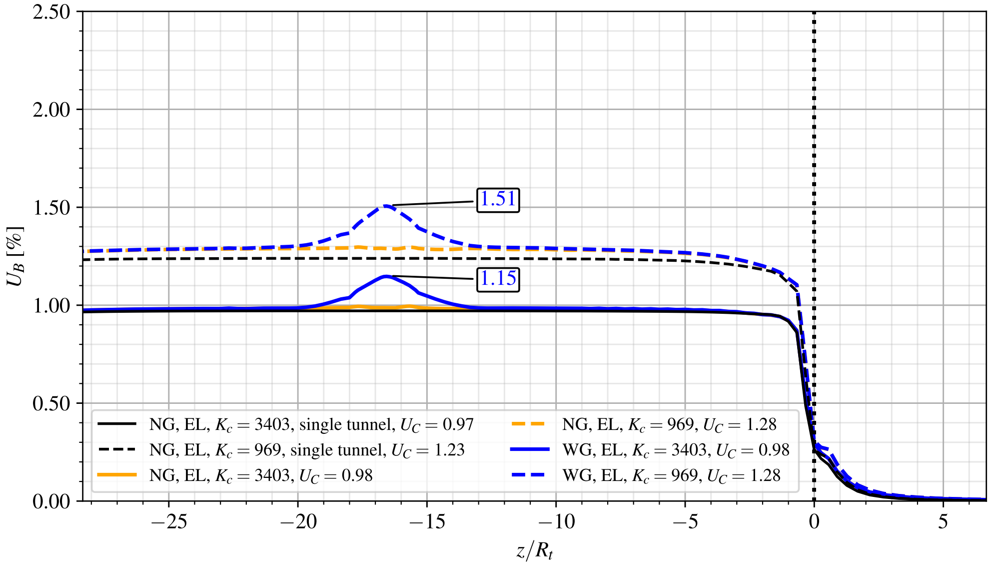

Figure 35: Effect of lining stiffness on the long-term convergence profiles for the configuration of twin tunnels with and without transverse gallery and distance between twin tunnels $d_1 = 4R_t$ - elastoplastic-viscoplastic rock mass, without and with elastic lining.

Overall, the same observations formulated in the previous analyses regarding the effect of twin tunnel spacing on stabilized convergence still hold: with respect to single tunnel configuration, U_C is almost unaffected by the lining stiffness for U_C and slightly increased (up to 4%) for $d_1 = 4R_t$.

With the elastic lining, the increase in stiffness from $K_{c_{28}} = 970$ MPa to $K_{c_{28}} = 3400$ MPa leads to a reduction in stabilized convergence U_C by 28% for twin tunnels spacing $d_1 = 16R_t$ and by 16% for $d_1 = 4R_t$, emphasizing once again the strong mechanical interaction between the different components of the tunnel structure.

The peak value of tunnel roof convergence U_{peak} that reflects the coupling associated with intersecting transverse gallery the coupling associated then intersecting is almost unaffected by the lining stiffness, at least for considered data parameters. In that respect, the value of ratio $(U_{peak} - U_C)/U_C$ computed in the configuration $d_1 = 16R_t$ (resp. $d_1 = 4R_t$) is approximately 12% (resp. and 18%) for both values of lining stiffness, which corroborates the predominating effect of tunnels proximity on peak convergence U_{peak}.

8. Conclusions

In general, the field of deformations and stresses around a deep tunnel depends on several interrelated factors, including the tunnel depth, anisotropy of in situ stresses, tunnel wall geometry, tunneling conditions, and the mechanical behavior and coupling of the rock mass and the lining. In twin tunnels, there is also the interaction due to the proximity between the tunnels and, if present, transverse galleries, which cause localized stress distribution and overloading the main tunnels. Furthermore, unlike single tunnels, the gallery's influence can only be studied with three-dimensional models.

One of the contributions of this study at the structural level is the development of a model capable of performing three-dimensional finite element simulations for a domain of deep circular twin tunnels with a transverse gallery. The construction process, including excavation and lining installation, was simulated using an activation/deactivation technique. At the material level, four constitutive models for the rock mass were implemented and investigated: elastic (E), elastoplastic (EP), viscoplastic (VP), and elastoplastic-viscoplastic (EPVP) model. For the lining, three configurations were considered: no lining (NL), elastic (EL), and viscoelastic (VEL) lining. In the numerical application of this study, the influence of different constitutive models was explored, as well as the effect of the spacing between axes of the longitudinal tunnels ($d_1 = 16R_t$, $8R_t$ and $4R_t$ where R_t is the tunnel radius) and the impact of lining stiffness on deformation control. For time-dependent models (which account for rock mass creep and lining creep and shrinkage), results were obtained and analyzed at the end of tunnel construction (short-term - ST) and after viscous effects had reached equilibrium (long-term - LT).

However, before this application, preliminary numerical simulations of the 3D computational model were carried out, and comparisons were made with analytical solutions for unlined twin tunnels under plane strain conditions, considering both elastic and elastoplastic rock mass. These simulations demonstrated the model's capacity to accurately capture the main effects occurring in such structures, including the ovalization effect, stress distribution, and the extent of the plastic zone, for various tunnel spacing, initial in situ stresses, and different values of cohesion and friction angle.

Regarding the application of this study, the main objective was to demonstrate the capability of the proposed formulation to address the three-dimensional problem of twin tunnels connected to galleries, involving nonlinear and time-dependent behaviors. However, a comprehensive parametric analysis that integrates the effects of geometric, constitutive, and loading parameters is beyond the scope of this specific numerical application. Constitutive parameters were selected for deep clay rockmass (at a depth of 450 m) from the eastern Paris basin, based on laboratory tests conducted under undrained conditions, which exhibited both instantaneous and delayed behavior and could be simulated by the implemented constitutive models. For the lining of both the twin tunnels and the gallery, a constitutive model values was used that takes into account the creep and shrinkage of concrete, through a viscoelastic aging model.

Considering the constitutive parameters and tunneling conditions adopted, some conclusions from this study can be highlighted. First, when comparing the convergence profiles, the difference between short-term and long-term responses is more pronounced when the lining is viscoelastic. This demonstrates the importance of adopting a model that accounts for concrete creep and shrinkage. The relatively high stiffness of an elastic lining significantly reduces the viscous deformations of the rock mass. In the short-term, the early age of the lining results in a lower relaxation modulus compared to the constant 28-day modulus used for the elastic lining. In the long-term, although the viscoelastic lining shows an increase in the relaxation modulus due to the aging phenomenon, the creep of both the rock and the lining components results in significantly greater convergences compared to models that do not consider time-delayed effects.

Additionally, the results indicate that the ovalization effect on the tunnel wall, caused by the proximity between the tunnels, is more pronounced in the short-term. Results with elastic lining showed that, over time, the viscosity of the rock mass tends to reduce this ovalization effect. The impact on tunnel convergence, due to the proximity of the tunnels d_1 and the time required for the complete excavation of the gallery, which also depends on this distance, was most significant for $d_1 = 4R_t$. This distance resulted in the highest peak convergence value at the roof of the longitudinal tunnel, located at the intersection of the twin tunnels and the gallery axes, represented by U_{peak}. Furthermore, a significant increase in the magnitude of U_{peak} between the short-term and long-term responses was observed, due to the influence of the time-dependent behavior of the rock and the concrete lining.

To assess the effect of the lining stiffness on deformation control, complementary analyses were carried out by reducing the lining thickness from $0.1R_t$ (higher stiffness) to $0.03R_t$ (moderate stiffness). Considering the elastoplastic behavior of the rock mass and elastic lining, the stiffer lining resulted in a 35% reduction in convergence compared to the unlined structure, while the moderate stiffness lining reduced convergence by only 12%. Regarding the influence zone of the gallery on the longitudinal tunnel convergence profile, it was observed that increasing the stiffness reduced the extent of this zone in all studied configurations ($22.5R_g$, without lining, $10.5R_g$ and $7.5R_g$ for stiffer and moderate stiffness lining, respectively, where R_g is the gallery radius). However, the spacing d_1 between the tunnels had little impact in extent of this zone. In terms of the displacements magnitude due to the presence of the gallery, in the configuration with the largest spacing $d_1 = 16R_t$, where less interaction between the twin tunnels is expected, the relative variation between the peak convergence U_{peak} and the convergence outside the gallery's influence zone U_c was approximately 14% for the unlined structure, 12.5% for the moderate stiffness lining, and 8.7% for the stiffer lining. These values were reduced to 9.7%, 13%, and 12%, respectively, for the spacing of $d_1 = 4R_t$, where the effects of lining stiffness and tunnel proximity occur simultaneously.

When the rock mass is elastoplastic-viscoplastic, long-term results suggest that the extent of the gallery's influence zone is also not affected by the distance d_1. However, the difference between the peak convergence U_{peak} and the convergence outside of this influence zone U_c is significantly influenced by d_1 and the stiffness of the lining. For an elastic lining, this difference is 12% for $d_1 = 16R_t$ and 18% for $d_1 = 4R_t$. This confirms that the effect of tunnel proximity on peak convergence is predominant. However, when the lining is viscoelastic, the stiffness of the lining significantly influences this difference. For $d_1 = 16R_t$, the values are 9.5% for the moderate stiffness lining and 13%

for the stiffer lining. For $d_1 = 4R_t$, these values are 14.5% and 18%, respectively, indicating the complex interaction between tunnel proximity, the gallery, and constitutive behaviors.

Although the conclusions are constrained by the validity of the models, the parameters adopted, and the tunneling conditions (such as the simultaneous excavation of longitudinal tunnels at a constant speed) the formulation and domain discretization employed proved effective in producing analyses involving twin tunnels with transverse gallery. However, additional validations through case studies are necessary to support the results of this study. Nonetheless, future developments are important and could expand this study. From a structural level, other tunneling conditions can be considered, such as the lagged distance between tunnels face or examining the impact of the proximity of these faces on the convergence of the gallery. Another aspect, relevant to time-dependent behavior, is to simulate the excavation of the tunnels and gallery with variable excavation speeds. On a material level, incorporating the effects of rock pore pressure and rock bolts through homogenization technique would improve the analysis.

References

[1] Karakus M, Ozsan A, Başarır H. Finite element analysis for the twin metro tunnel constructed in Ankara Clay, Turkey. Bulletin of Engineering Geology and the Environment 2007;66(1):71–79. URL: http://link.springer.com/10.1007/s10064-006-0056-z. doi:10.1007/s10064-006-0056-z.

[2] Zheng G, Zhang T, Diao Y. Mechanism and countermeasures of preceding tunnel distortion induced by succeeding EPBS tunnelling in close proximity. Computers and Geotechnics 2015;66:53–65. URL: https://www.sciencedirect.com/science/article/pii/S0266352X15000105. doi:https://doi.org/10.1016/j.compgeo.2015.01.008.

[3] Do NA, Dias D, Oreste P. 3D numerical investigation of mechanized twin tunnels in soft ground – Influence of lagging distance between two tunnel faces. Engineering Structures 2016;109:117–125. URL: https://linkinghub.elsevier.com/retrieve/pii/S0141029615007609. doi:10.1016/j.engstruct.2015.11.053.

[4] Forsat M, Taghipoor M, Palassi M. 3D FEM Model on the Parameters' Influence of EPB-TBM on Settlements of Single and Twin Metro Tunnels During Construction. International Journal of Pavement Research and Technology 2022;15(3):525–538. URL: https://link.springer.com/10.1007/s42947-021-00034-0. doi:10.1007/s42947-021-00034-0.

[5] Phutthananon C, Lertkultanon S, Jongpradist P, Duangsano O, Likitlersuang S, Jamsawang P. Numerical investigation on the responses of existing single piles due to adjacent twin tunneling considering the lagging distance. Underground Space 2023;11:171–188. URL: https://www.sciencedirect.com/science/article/pii/S2467967423000387. doi:https://doi.org/10.1016/j.undsp.2022.12.005.

[6] Islam MS, Iskander M. Twin tunnelling induced ground settlements: A review. Tunnelling and Underground Space Technology 2021;110:103614. URL: https://www.sciencedirect.com/science/article/pii/S088677982030568X. doi:https://doi.org/10.1016/j.tust.2020.103614.

[7] Chen F, Lin Lb, Li D. Analytic solutions for twin tunneling at great depth considering liner installation and mutual interaction between geomaterial and liners. Applied Mathematical Modelling 2019;73. doi:https://doi.org/10.1016/j.apm.2019.04.026.

[8] Ma Y, Lu A, Zeng X, Cai H. Analytical solution for determining the plastic zones around twin circular tunnels excavated at great depth. International Journal of Rock Mechanics and Mining Sciences 2020;136:104475. doi:https://doi.org/10.1016/j.ijrmms.2020.104475.

[9] Guo Z, Liu X, Zhu Z. An elastic solution for twin circular tunnels' stress in hydrostatic stress field. Geotechnical and Geological Engineering 2021;39:1–11. doi:https://doi.org/10.1007/s10706-021-01756-5.

[10] Fortsakis P, Bekri E, Prountzopoulos G, Marinos P. Numerical analysis of twin tunnels interaction. In: Proc. 1st Eastern European Tunnelling Conference. Budapest, Hungary; 2012,.

[11] Chortis F, Kavvadas M. Three-dimensional numerical investigation of the interaction between twin tunnels. Geotechnical and Geological Engineering 2021;39:5559–5585. doi:https://doi.org/10.1007/s10706-021-01845-5.

[12] Chortis F, Kavvadas M. Three-dimensional numerical analyses of perpendicular tunnel intersections. Geotechnical and Geological Engineering 2021;39:1771–1793. doi:https://doi.org/10.1007/s10706-020-01587-w.

[13] Chortis F, Kavvadas M. 3D numerical investigation of the axial forces acting on tunnel junctions constructed in fractured/weathered to very blocky rockmass. In: Expanding Underground-Knowledge and Passion to Make a Positive Impact on the World. CRC Press; 2023, p. 1574–1582.

[14] Chortis F, Kavvadas M. 3D numerical investigation of the bending moments acting on tunnel junctions constructed in fractured/weathered to very blocky rockmass. In: Expanding Underground-Knowledge and Passion to Make a Positive Impact on the World. CRC Press; 2023, p. 1583–1591.

[15] Bažant ZP, Prasannan S. Solidification theory for concrete creep. I: Formulation. Journal of Engineering Mechanics 1989;115(8):1691–1703. doi:https://doi.org/10.1061/(ASCE)0733-9399(1989)115:8(1691).

[16] Bažant ZP, Prasannan S. Solidification theory for concrete creep. II: Verification and application. Journal of Engineering Mechanics 1989;115(8):1704–1725. doi:https://doi.org/10.1061/(ASCE)0733-9399(1989)115:8(1704).

[17] ANSYS. ANSYS Programmer's Reference, release 15.0. Canonsburg, Pennsylvania; 2013.

[18] Nemat-Nasser S, Hori M. Micromechanics: overall properties of heterogeneous materials. North-Holland; 1993.

[19] Deudé V, Dormieux L, Kondo D, Maghous S. Micromechanical approach to nonlinear poroelasticity: Application to cracked rocks. Journal of Engineering Mechanics 2002;128(8):848–855. doi:https://doi.org/10.1061/(ASCE)0733-9399(2002)128:8(848).

[20] de Buhan P, Fréard J, Garnier D, Maghous S. Failure properties of fractured rock masses as anisotropic homogenized media. Journal of Engineering Mechanics 2002;128(8):869–875. doi:https://doi.org/10.1061/(ASCE)0733-9399(2002)128:8(869).
[21] Marmier R, Jeannin L, Barthélémy JF. Homogenized constitutive laws for rocks with elastoplastic fractures. International Journal for Numerical and Analytical Methods in Geomechanics 2007;31(10):1217–1237. doi:https://doi.org/10.1002/nag.595.
[22] Aguiar CB, Maghous S. A micromechanics-based approach to damage propagation criterion in viscoelastic fractured materials regarded as homogenized media. International Journal for Numerical and Analytical Methods in Geomechanics 2023;47(6):936–971. doi:https://doi.org/10.1002/nag.3500.
[23] Rousset G. Comportement mecanique des argiles profondes: Application au stockage de déchets radioactifts. Ph.D. Thesis (in french); Ecole Nationale des Ponts et Chaussées; Paris, France; 1988. URL: https://theses.hal.science/tel-00529719/.
[24] Nguyen Minh D, Rousset G. Influence of instantaneous failure on time dependent behavior of underground galleries. In: The 28th U.S. Symposium on Rock Mechanics (USRMS). Tucson, Arizona; 1987, p. ARMA–87–0663. URL: https://onepetro.org/ARMAUSRMS/proceedings-abstract/ARMA87/All-ARMA87/129838.
[25] Giraud A, Rousset G. Time-dependent behaviour of deep clays. Engineering Geology 1996;41(1):181–195. doi:https://doi.org/10.1016/0013-7952(95)00000-3.
[26] Bernaud D, Rousset G. L'essai de soutènement à convergence controlée. In: Proc. of International Symposium, Geotechnical Engineering of Hard Soils-Soft Rocks. Athens; 1993, p. 1381–1391.
[27] Piepi GT. Comportement viscoplastique avec rupture des argiles raides. applications aux ouvrages souterrains. Ph.D. Thesis (in french); Ecole Nationale des Ponts et Chaussées; Paris, France; 1995. URL: https://pastel.hal.science/tel-00523616/document.
[28] Quevedo FPM. Análise computacional das deformações em túneis profundos considerando o acoplamento plasticidade-viscoplasticidade. Ph.D. Thesis (in portuguese); Federal University of Rio Grande do Sul; Porto Alegre, Brazil; 2021. URL: https://lume.ufrgs.br/handle/10183/239617.
[29] Quevedo FPM, Bernaud D, Maghous S. Numerical integration scheme for coupled elastoplastic–viscoplastic constitutive law for tunnels. International Journal of Geomechanics 2022;22(10). doi:https://doi.org/10.1061/(ASCE)GM.1943-5622.0002512.
[30] Bernaud D. Tunnels profonds dans les milieux viscoplastiques: approches expérimentale et numérique. Ph.D. Thesis (in french); Ecole Nationale des Ponts et Chaussées; Paris, France; 1991. URL: https://theses.hal.science/tel-00529719/.
[31] Perzyna P. Fundamental problems in viscoplasticity. In: Advances in applied mechanics; vol. 9. Elsevier; 1966, p. 243–377.
[32] CEB-FIP . CEB-FIP model code 1990: Design code. Comité Euro International du Béton and Fédération Internationale de la Précontrainte (CEB-FIP); 1993.
[33] Quevedo FPM, Schmitz RJ, Morsch IB, A. CF, Bernaud D. Customization of a software of finite elements to analysis of concrete structures: long-term effects. IBRACON Structures and Materials Journal 2018;11(4):696–718. doi:https://doi.org/10.1590/S1983-41952018000400005.
[34] Quevedo FPM, Bernaud D, Campos Filho A. Numerical analysis of deep tunnels in viscoplastic rock mass considering the creep and shrinkage of the concrete lining. International Journal of Geomechanics 2022;22(4). doi:https://doi.org/10.1061/(ASCE)GM.1943-5622.0002282.
[35] Quevedo FPM. Comportamento a longo prazo de túneis profundos revestidos com concreto: modelo em elementos finitos. Master Thesis (in portuguese); Federal University of Rio Grande do Sul; Porto Alegre, Brazil; 2017. URL: https://lume.ufrgs.br/handle/10183/163886.
[36] Bernaud D, Debuhan P, Maghous S. Numerical-simulation of the convergence of a bolt-supported tunnel through a homogenization method. International Journal for Numerical and Analytical Methods in Geomechanics 1995;19(4):267–288. doi:https://doi.org/10.1002/nag.1610190404.
[37] Bernaud D, Maghous S, Debuhan P, Couto E. A numerical approach for design of bolt-supported tunnels regarded as homogenized structures. Tunneling and underground space technology 2009;24(5):533–546. doi:https://doi.org/10.1016/j.tust.2009.02.002.
[38] Maghous S, Bernaud D, Couto E. Three-dimensional numerical simulation of rock deformation in bolt-supported tunnels: A homogenization approach. Tunneling and Underground Space Technology 2012;31:267–288. doi:https://doi.org/10.1016/j.tust.2012.04.008.
[39] Zienkiewicz O, Cormeau I. Visco-plasticity—plasticity and creep in elastic solids—a unified numerical solution approach. International Journal for Numerical Methods in Engineering 1974;8(4):821–845. doi:https://doi.org/10.1002/nme.v8:4.
[40] Simo JC, Hughes TJR. Computational Inelasticity. Springer-Verlag; 1998.
[41] Ling C. On the stresses in a plate containing two circular holes. Journal of Applied Physics 1948;19(1):77–82. doi:https://doi.org/10.1063/1.1697875.
[42] Giraud A. Couplages thermo-hydro-mécaniques dans les poreux peu perméables: application aux argiles profondes. Ph.D. Thesis (in french); Ecole Nationale des Ponts et Chaussées; Paris, France; 1993. URL: https://theses.fr/1993ENPC9310.
[43] Panet M. Le Calcul des Tunnels par la Méthode Convergence-Confinement. Presses De L'ecole Nationale Des Ponts Et Chaussees; 1995. ISBN 2859782303.
[44] Hoek E, Brown ET. Underground excavations in rock. CRC Press; 1980.